

Direct numerical simulation of turbulent flow in a square duct

By ASMUND HUSER† AND SEDAT BIRINGEN

Department of Aerospace Engineering Sciences, University of Colorado, Boulder,
CO 80309, USA

(Received 22 May 1992 and in revised form 3 March 1993)

A direct numerical simulation of a fully developed, low-Reynolds-number turbulent flow in a square duct is presented. The numerical scheme employs a time-splitting method to integrate the three-dimensional, incompressible Navier–Stokes equations using spectral/high-order finite-difference discretization on a staggered mesh; the nonlinear terms are represented by fifth-order upwind-biased finite differences. The unsteady flow field was simulated at a Reynolds number of 600 based on the mean friction velocity and the duct width, using $96 \times 101 \times 101$ grid points. Turbulence statistics from the fully developed turbulent field are compared with existing experimental and numerical square duct data, providing good qualitative agreement. Results from the present study furnish the details of the corner effects and near-wall effects in this complex turbulent flow field; also included is a detailed description of the terms in the Reynolds-averaged streamwise momentum and vorticity equations. Mechanisms responsible for the generation of the stress-driven secondary flow are studied by quadrant analysis and by analysing the instantaneous turbulence structures. It is demonstrated that the mean secondary flow pattern, the distorted isotachs and the anisotropic Reynolds stress distribution can be explained by the preferred location of an ejection structure near the corner and the interaction between bursts from the two intersecting walls. Corner effects are also manifested in the behaviour of the pressure–strain and velocity–pressure gradient correlations.

1. Introduction

Turbulent flow along a streamwise corner is of considerable engineering interest, with relevance to flow in the root region of a lifting section, complex flow in turbomachinery and heat exchangers, flows in ducts with non-circular cross-section, and flows in open channels and rivers. These complex turbulent flows have two inhomogeneous directions and are characterized by the existence of secondary flows of the second kind (as classified by Prandtl 1926) which are secondary mean flows created by the turbulent motion. Although this type of secondary flow is relatively weak (about 2–3% of the streamwise bulk velocity), its effects on wall shear stress distribution, heat transfer rates, or transport of passive tracers are quite significant (Demuren 1990). Secondary flow of the second kind is most frequently studied by considering turbulent flow in a square duct because of its relatively simple geometry which also provides an excellent case to test and develop turbulence models. The mean transverse secondary flow that occurs in this geometry is well defined and consists of eight streamwise vortices, two counter-rotating in each corner, with the flow directed toward the corners from the duct centre along the corner bisector, and toward the duct centre along the

† Current address: DNV Technica, N-1322 Høvik, Norway.

wall bisector. An explanation of the origin of secondary flows of the second kind was first offered by Prandtl (1926), who suggested that in a region of isotach curvature, secondary flows are created by turbulent velocity fluctuations. Prandtl postulated that in these regions velocity fluctuations are greater parallel to the isotachs than normal to the isotachs, causing flow toward the concave side of the isotachs. In a later description, Prandtl (1952) explained the distorted isotachs by the convection of mean velocity toward regions with low shear (e.g. along the corner bisector in square duct flow) from regions with high shear (e.g. along the walls in square duct flow). This results in an increased mean velocity along the corner bisector and reduced mean velocity near the wall bisector (as opposed to laminar flow), as first documented experimentally by Nikuradse (1930). In order to investigate the convection of mean streamwise velocity by the secondary flow, Gessner (1973) analysed the terms in the total kinetic energy equation along the corner bisector. Accordingly, energy loss due to a positive turbulent shear stress gradient along the corner bisector is compensated by an increase in total energy in the streamwise mean velocity. Gessner (1973) concluded that the anisotropy of the primary shear stress is the main cause of the increased streamwise velocity in the corners.

A review of experimental work and turbulence models describing secondary flows is given by Demuren & Rodi (1984). In their study, calculations were performed using an algebraic Reynolds stress model. The results showed the difficulties involved in modelling the secondary flows produced by a fine balance between the secondary Reynolds stress gradients.

Experimental studies of simple turbulent shear flows have demonstrated that streamwise vorticity is primarily created during a bursting event observed as low-speed streaks and ejections (Kline *et al.* 1967). In the square duct flow, bursting is also the dominating event. Secondary flow of the second kind contains mean streamwise vortices, produced by three-dimensional mean strain rates. Although significant effort has been devoted into the physical and phenomenological description of secondary flows of the second kind, a satisfactory explanation of the mechanisms causing these effects is still not available; consequently no turbulence model at the present time is fully capable of predicting the turbulence characteristics of secondary flows. Because the bursting event is central to turbulence production (Lumley 1991) and because the ejection structure contains most of the turbulence energy (Moin & Moser 1989), in the present work we attempt to explain the creation of mean streamwise vortices in the square duct flow by analysing these processes.

Direct numerical simulation (DNS) of simple shear flows has proven to be an effective and important tool for studying turbulence structures and near-wall effects. Used in connection with experiments and theoretical models, DNS provides turbulence modellers with the ability to validate concepts and theories (Launder 1990). Earlier DNS work has primarily concentrated on turbulent channel flow (Kim, Moin & Moser 1987) and zero-pressure-gradient boundary layer (Spalart 1985), documenting near-wall effects on turbulent wall-bounded flows with one inhomogeneous direction. Moser & Moin (1987) performed the DNS of a curved channel flow, highlighting the centrifugal force influence on turbulent channel flow. In contrast to these studies, in which there is only one inhomogeneous direction, the present work considers a geometry with two inhomogeneous directions and focuses on 'new' effects resulting from the complex interaction of turbulence structures in the vicinity of the corners. The description of these new effects motivates the present work, leading to the cause of the distorted isotachs and the creation of mean secondary flows. Simultaneously with the present work, Gavrilakis (1992) performed a DNS of the square duct at a low Reynolds

number, providing a detailed description of the mean flow in the transverse plane and turbulence statistics along the wall bisector. Gavrilakis (1992) also calculated the terms in the mean streamwise vorticity equation, but did not report the mechanisms responsible for the new effects due to the presence of the corner.

The objective of this work is to develop an efficient numerical solution procedure for the three-dimensional, time-dependent, incompressible Navier–Stokes equations and to perform a DNS of the square duct flow at a Reynolds number in the well-established turbulent regime, providing a database from which turbulence statistics and the characteristics of the Reynolds-averaged flow field are obtained. The DNS data base is then used to provide a detailed description of the corner influence on turbulence statistics and on the origin of the secondary flows of the second kind.

2. Problem definition and scales

We consider fully developed, incompressible turbulent flow in a square duct; the geometry and coordinate system are displayed in figure 1. The governing equations are the three-dimensional, time-dependent Navier–Stokes equations,

$$\frac{\partial \mathbf{u}}{\partial t} + \mathbf{u} \cdot \nabla \mathbf{u} = -\nabla p + \frac{1}{Re_\tau} \nabla^2 \mathbf{u} + 4\mathbf{i}, \quad (1)$$

and the continuity equation,

$$\nabla \cdot \mathbf{u} = 0. \quad (2)$$

Equations (1) and (2) are written in non-dimensional form, where the mean friction velocity, u_τ , and the duct width, D , are used as the velocity and length scales, respectively. With this non-dimensionalization, the Reynolds number is defined as $Re_\tau = u_\tau D/\nu$. The length scale used here is the hydraulic diameter and this is four times the hydraulic radius, which is the length scale commonly used in channel flow ($D = 4\delta$). The kinematic viscosity is given by ν ; the mean pressure gradient is $-4\mathbf{i}$, where \mathbf{i} represents the unit vector in the streamwise direction; the fluctuating pressure is given by $p = P/(\rho u_\tau^2)$, where P is the dimensional pressure and ρ is the density. No-slip boundary conditions are imposed on the solid walls and the flow is assumed to be periodic in the x -direction.

The data base used in the present work was obtained from two runs, the computational parameters for which are given in table 1. The Reynolds number in both calculations was $Re_\tau = 600$ which is in the fully developed turbulent regime. The following algebraic stretching was implemented along the wall-normal directions (Anderson, Tennehill & Pletcher 1984, p. 249),

$$y_j = \frac{1}{2}(b-1) \left[\frac{a^{2j/N_y} - 1}{a^{(2j/N_y - 1)} + 1} \right], \quad j = 0, 1, \dots, N_y, \quad (3)$$

where $a = (b+1)/(b-1)$, N_y is the number of grid points in the y -direction and $b = 1.1$ is a stretching parameter. Figure 2 displays the energy spectra for the coarse grid calculation (Run A, table 1) obtained at points along the wall bisector; in this figure α_x is the x -directional wavenumber, $\alpha_x = 2\pi n/l_x$, $n = 0, 1, \dots, \frac{1}{2}N_x - 1$, where $l_x = L_x/D$ is the non-dimensional computational box length and N_x is the number of grid points along the x -direction. This figure exhibits only a marginal buildup of energy in the high wavenumbers, indicating that even at this low resolution, the present numerical code accurately captures the energy spectra, especially for the large-scale effects.

The streamwise two-point correlation lengths represent the characteristic length of the longest turbulence structures in the streamwise direction and the computational

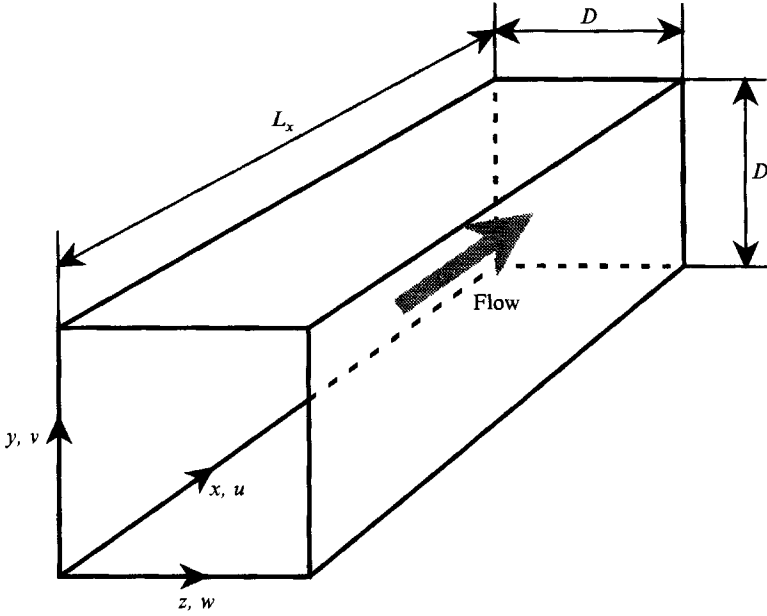


FIGURE 1. Geometry and coordinate system.

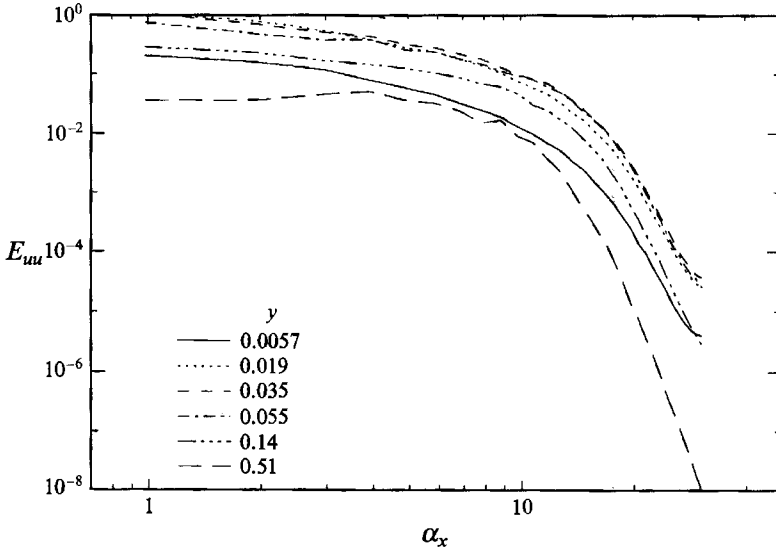


FIGURE 2. Energy spectra, E_{uu} , at selected points along the wall bisector; $z = 0.51$.

Run	Grid	t_{tot}	Δt	Re_B
A	$81 \times 81 \times 64$	15	0.001	10620
B	$100 \times 100 \times 96$	10	0.0008	10320

TABLE 1. Computational parameters and bulk Reynolds numbers from runs A and B.
 $Re_r = 600, l_z = 6.4$.

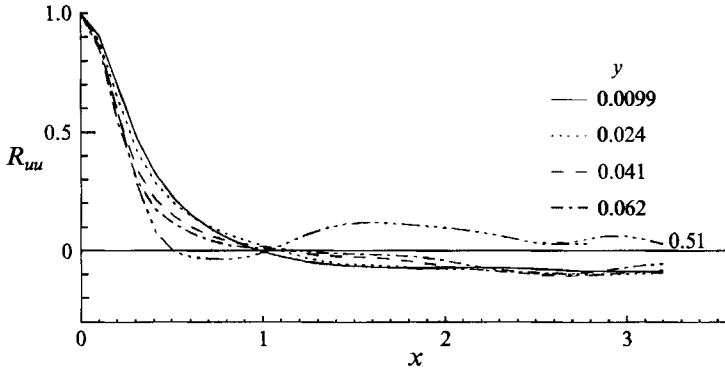


FIGURE 3. Two-point correlation coefficient, R_{uu} , at selected points along the wall bisector; $z = 0.51$.

domain must be able to capture these structures. Sample results from the present coarse-grid calculations indicate that the correlation coefficients are close to zero at $x = \frac{1}{2}l_x = 3.2$ (figure 3). Consequently no further computer resources were committed to study the influence of the domain length and $l_x = 6.4$ was used throughout this work. In comparison, in the recent study of Gavrilakis (1992) a box length of $l_x = 31.4$ was used, whereas the large-eddy simulation of Madabhushi & Vanka (1991) was performed with $l_x = 6.4$, as in the present work. On the basis of very favourable comparisons of the present results with existing square duct and channel flow data we assert that the influence of the shorter computational domain is marginal in the present calculations which accurately capture the characteristic effects creating secondary flows.

3. The numerical procedure

The Navier–Stokes equations, (1), and the continuity equation, (2), were advanced in time by using a time-splitting method (Kim & Moin 1984) improved with a Runge–Kutta formulation of the time-stepping procedure (Le & Moin 1991). The time-splitting method involves uncoupling of (1) and (2) so that first, the momentum equations are solved independently of the pressure field, and second the velocities are corrected by a pseudo-pressure field, which satisfies a divergence-free velocity field. With the Runge–Kutta formulation, the uncoupled Navier–Stokes equations are obtained as

$$\frac{\hat{u}^m - u^{m-1}}{\Delta t} = \gamma_m N^{m-1} + \zeta_m N^{m-2} + 4i + \frac{\beta_m}{Re_\tau} \nabla_{yz}^2 (u^m + \hat{u}^{m-1}), \quad (4)$$

$$\frac{u^m - \hat{u}^m}{\Delta t} = -\nabla \phi^m. \quad (5)$$

Here \hat{u}^m is the intermediate velocity field; $m = 1, 2, 3$ denote the substeps in the Runge–Kutta scheme. The superscript $m-1$ denotes the last substep in the previous time-step, Δt is the total Runge–Kutta time step, $N = -\partial(u_i u_j)/\partial x_j + (1/Re_\tau)(\partial^2 u/\partial x^2)$ contains the nonlinear terms and the x -directional viscous diffusion term, with the nonlinear terms written in index notation; the coefficients β , γ , and ζ assume constant values at each Runge–Kutta substep and these values are given elsewhere (Le & Moin 1991). The diffusion operator, $\nabla_{yz}^2 = \partial^2/\partial y^2 + \partial^2/\partial z^2$, is applied only along the wall-normal directions. The x -directional diffusion term is solved explicitly together with the

nonlinear terms in order to save storage and computer time. With this Runge–Kutta scheme, numerical stability was maintained up to a Courant number, $C \leq 4$. This Courant number is greater than the upper limit obtained from the linear stability analysis (Le & Moin 1991) which is $C \leq \sqrt{3}$, indicating that this linear criterion is not very strict in the calculation of the present flow. Calculations performed with smaller time steps corresponding to $C \leq \sqrt{3}$ gave identical results with $C \leq 4$ indicating the time accuracy of the present results.

Boundary conditions for the intermediate velocities parallel to the walls are given by $\mathbf{u} \cdot \mathbf{p} = 0$, where \mathbf{p} denotes the unit direction parallel to the walls. No corrections were applied to the intermediate slip velocities, as the present non-corrected boundary conditions were found to introduce negligible errors in previous studies (Huser & Biringen 1992; Gresho 1990).

All the finite differences used to represent the first and second derivatives in the wall-normal directions were obtained by a Lagrangian polynomial method developed in this work. This method obtains the finite-difference coefficients of any order on a stretched, staggered grid, including one-sided and biased differences (Huser 1992).

The convective (nonlinear) terms, represented by $\partial(u_i u_j)/\partial x_j$, are responsible for transporting energy in the wavenumber space causing aliasing errors whenever spectral or finite-difference methods are used to discretize these terms when the finest scales are not resolved. According to Rai & Moin (1991), these errors can be minimized by using high-order upwind-biased finite differences as opposed to central differences and spectral methods. Consequently, in the present simulations, fifth-order upwind-biased differences were used for the convective terms in all the three directions.

The time-splitting method involves the implicit solution of the momentum and the pressure equations which are Helmholtz- and Poisson-type equations, respectively. These equations were efficiently solved by the tensor product method (Huser & Biringen 1992). The momentum equations were solved by using fourth-order central differences for the viscous terms providing a nine-point stencil in the wall-normal directions. Along the streamwise direction, because the flow is periodic, the pseudo-spectral Fourier method was implemented to calculate the viscous terms and to solve the pseudo-pressure equation. When discretizing the pseudo-pressure equation in the wall-normal directions, fourth-order central differences were used, and the coefficient matrices were constructed by applying consistent divergence (div) and gradient (grad) operators on a staggered mesh. The second-derivative operator was found by combining the div and the grad operators resulting in the use of a 13-point stencil for the interior points in the wall-normal directions. By using consistent operators in the pseudo-pressure equation and when updating the velocities, divergence was satisfied to machine accuracy. The details of the application of this method to the present problem are available in Huser (1992).

A low-order version of the solution procedure was tested extensively on two-dimensional cavity problems, obtaining good agreement with bench-mark solutions (Huser & Biringen 1992).

4. Turbulence statistics and mean flow budgets

The fully developed flow in the duct was obtained by perturbing the laminar mean flow with a random velocity field, and the code was run until a statistically steady state was obtained. Steady state was reached after $t = Tu_\tau/D \approx 60$ time units and was identified by a constant mean value of the total kinetic energy and a linear mean shear stress profile. This transient period corresponds to a distance of about $1300D$ travelled

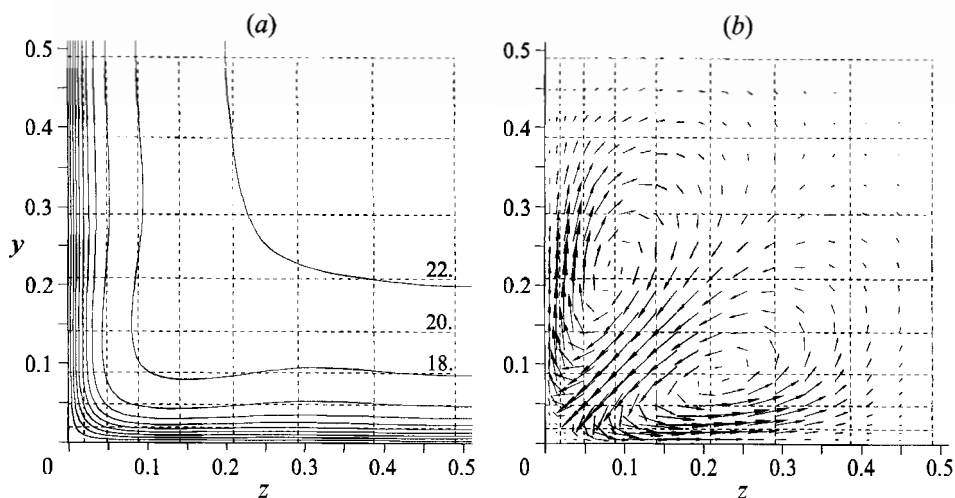


FIGURE 4. Ensemble-averaged mean velocities, Run A: (a) \bar{u} -contours, increment = 2; (b) \bar{v} , \bar{w} velocity vectors.

by a particle on the centreline of the duct. This distance is much longer than the entrance length which is about $80D$ (Gessner, Po & Emery 1979). Long-term statistics were obtained from runs A and B (table 1) when the flow was fully developed.

In this section we present the mean flow properties and one-point correlations from runs A and B which are compared with existing experimental and computational data. All the terms in the mean streamwise momentum and vorticity budgets are also presented. Specifically we focus on the effects of the corner on turbulent stress gradients and on the mean convection.

Long-term statistics were obtained by averaging the flow field in the homogeneous direction, x , and in time; in the following discussion, the averaged values are generally indicated by an overbar and a prime indicates turbulent fluctuation quantities.

4.1. Mean flow properties

The long-term statistics for Run A were obtained over a time-period ($t_{tot} = 15$) which corresponds to the time it would take a particle at the channel centre to travel a distance equal to about $330D$. The distributions are ensemble averaged over the eight similar triangles that form when the wall and corner bisectors are drawn. This resultant flow field is displayed in figure 4, in which only the lower left quadrant of the duct cross-section is shown. In order to obtain the best statistical averages, the mean properties were ensemble averaged when compared with experiments.

Figure 4(b) displays the secondary flow velocity vectors, revealing the two streamwise, counter-rotating vortices in each corner that characterize this flow. For the present low-Reynolds-number computations, the vortex centres are closer to the corner and the secondary flow is weaker near the wall bisector than in higher-Reynolds-number experiment (Brundrett & Baines 1964). Figure 4(a) shows that the isotachs are bent toward the corner, indicating a magnitude increase for \bar{u} . At the wall bisector, the present results exhibit a local maximum for \bar{u} whereas a local minimum exists in high-Reynolds-number experiments (Brundrett & Baines 1964) (table 2 lists the Reynolds numbers of the computational and experimental studies referred to in this paper). The occurrence of a local \bar{u} maximum at the wall bisector is a low-Reynolds-number effect (Gessner 1973; Gavrilakis 1992). By plotting the ensemble-averaged skin friction

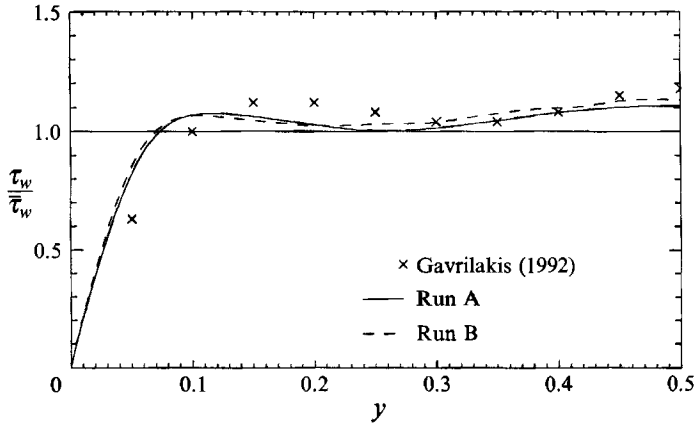


FIGURE 5. Ensemble-averaged wall stress variation.

Reference	Investigation	Re_B	Re_τ
Present, run B	duct, DNS	10320	600
Madabushi & Vanka (1991)	duct, LES	5810	360
Gavrilakis (1992)	duct, DNS	4410	300
Gessner <i>et al.</i> (1979)	duct, experiment	250000	10550
Brundrett & Bains (1964)	duct, experiment	83000	3860
Kim <i>et al.</i> (1987)	channel, DNS	13200	720
Balint <i>et al.</i> (1991)	boundary layer, experiment	$Re_\delta = 27650$	

TABLE 2. Works considered in this paper and their Reynolds numbers. The Reynolds number Re_δ is based on the boundary-layer thickness and the free-stream velocity.

variation as a function of the distance along the wall, it is observed that the local maximum in \bar{u} also yields a maximum in τ_w at the wall bisector (figure 5). In figure 5 the distribution of $\tau_w/\bar{\tau}_w$ obtained from the present simulations is compared with data from Gavrilakis (1992), which also attains its maximum value at the wall bisector. Variations between these distributions could be due to the Reynolds-number differences manifested by a steeper gradient in $\tau_w/\bar{\tau}_w$ towards the corner at the higher Reynolds number of the present study.

Except for a 2.8% difference in bulk Reynolds numbers (table 1), mean velocities obtained from the fine-grid calculation are very similar to the coarser grid results obtained in run A. The finer resolution in run B provides more accurate results indicated by a higher friction factor, which is $f = 8u_\tau^2/U_B^2 = 0.027$ in run B and $f = 0.026$ in run A. The experimentally found friction factor is $f = 0.030$ (Hartnett, Koh & McComas 1962).

The mean streamwise velocity profile along the wall bisector ($z = 0.5$) is plotted in wall coordinates in figure 6 and compared with the low-Reynolds-number large-eddy simulation of Madabhusli & Vanka (1991), and the data from the DNS of Gavrilakis (1992). The mean velocity profile is also compared with the law of the wall, which reads

$$\bar{u} = \frac{1}{\kappa} \ln y^+ + 5.5, \quad (6)$$

where $\kappa = 0.41$ is the von Kármán constant and $y^+ = yRe_\tau$. In figure 6, where the variables are normalized with the local friction velocity, the overshoot from the 'log

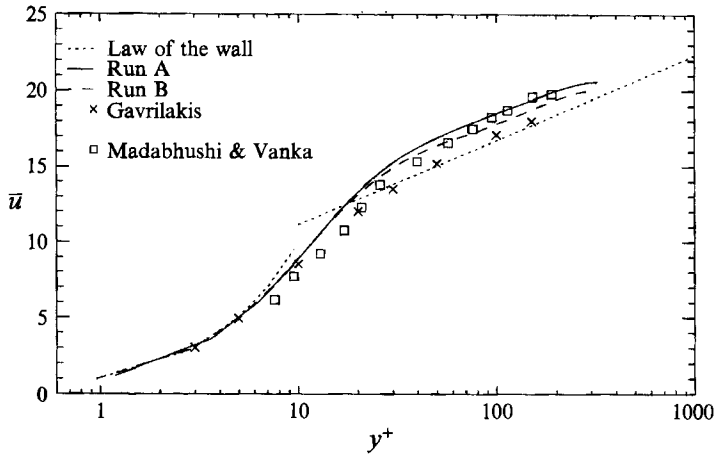


FIGURE 6. Comparing mean streamwise velocity along the wall bisector with the law of the wall and previous square duct work.

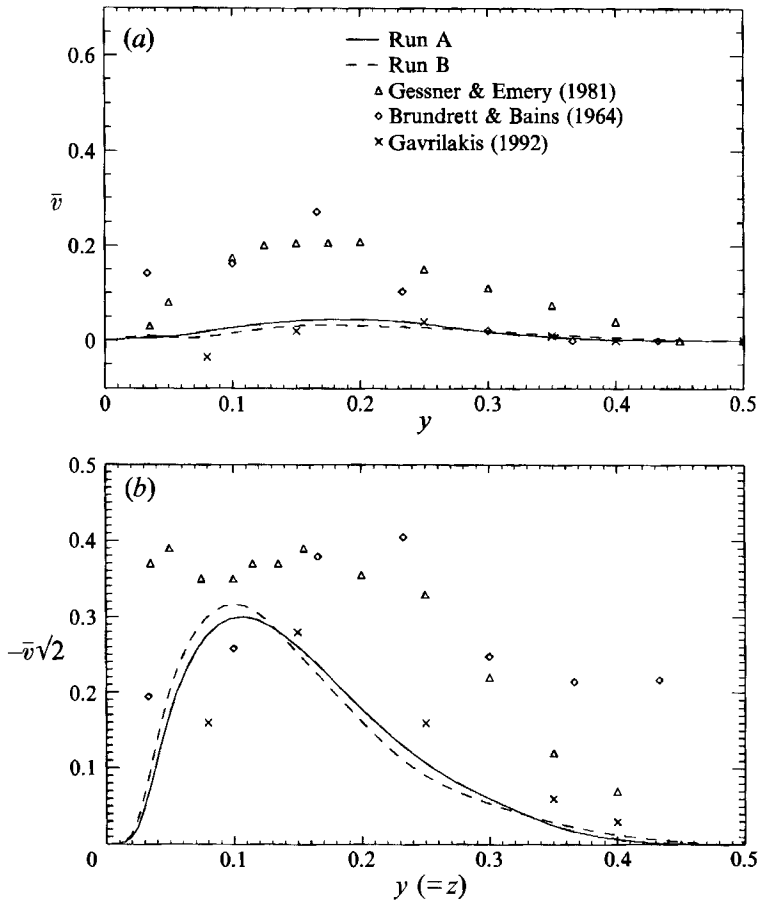


FIGURE 7. Comparison of secondary velocity vectors: (a) along the wall bisector; and (b) along the corner bisector.

law', (6), is likely the result of stronger turbulence production near the walls away from the corners in duct flow compared to channel and boundary-layer flows (see §4.2). Gavrilakis (1992) also argued that the square duct geometry influences the log law even though his data show a closer fit when normalized by the local friction velocity in figure 6. The coarse-grid resolution near the wall bisector (due to the stretched mesh parallel to the wall) may also have influenced the mean velocity profile in this region. In figure 6, a comparison between runs A and B reveals that the overshoot from the log law is slightly reduced with the finer grid.

In figure 7, the secondary velocity distributions along the corner and the wall bisector are compared with experiments (Brundrett & Baines 1964 and Gessner & Emery 1981) and simulations (Gavrilakis 1992). The present values of \bar{v} are significantly lower than the experimental results along the wall bisector (see figure 7a). In the low-Reynolds-number simulation of Gavrilakis (1992) negative \bar{v} are observed for $y < 0.1$, which do not exist in the present results where the Reynolds number is higher (see table 2). The low \bar{v} -velocity at the wall bisector in the present results is a low-Reynolds-number effect occurring together with the local maximum wall shear stress at this location. According to figure 7(b), the level of the secondary velocity along the corner bisector compares well with experiments. Using this velocity as a measure of the strength of the secondary flow, figure 7(b) indicates that when normalized by the mean friction velocity, the strength of the secondary flow is independent of the Reynolds number (Launder & Ying 1972). In figure 7, results from runs A and B are also compared, exhibiting a marginal difference.

4.2. Turbulence intensities

The near-wall behaviour of the turbulence intensities, normalized by the *local* friction velocity, is displayed in figure 8(a–c) where the y^+ distributions at the wall bisector are compared with data from the channel flow DNS (Kim *et al.* 1987), boundary-layer measurements (Balint, Wallace & Vukoslavčević 1991) and square duct DNS results (Gavrilakis 1992) (table 2). Figure 8(a–c) displays that in the viscous sublayer for $y^+ < 10$, turbulence intensities from the present calculations provide excellent agreement with the other data (Kim *et al.* 1987 and Gavrilakis), indicating the universality of the inner scaling here. Away from the wall, it is observed that the maximum value in u_{rms} is highest in the present square duct flow (figure 8a), whereas further away from the wall, in the log region ($y^+ > 40$), the boundary-layer flow (Balint *et al.* 1991) has the highest $\overline{u'^2}$ value. All the components of the turbulent intensity increase with the Reynolds number in the log region of wall-bounded turbulent flows (Willmarth 1975 and Balint *et al.* 1991). The differences in y^+ distributions outside the viscous sublayer in figure 8(a–c) could be the result of Reynolds-number differences, different flow-field geometries as well as numerical and experimental errors. In the present results the u_{rms} decrease with increasing grid resolution (figure 8a). This was also observed by Rai & Moin (1991), indicating that the upwind-biased scheme has a tendency to overpredict the maximum value in u_{rms} when the computation is under-resolved.

4.3. Mean streamwise momentum equation

For the square duct flow, the Reynolds-averaged streamwise momentum equation is written as

$$\bar{v} \frac{\partial \bar{u}}{\partial y} + \bar{w} \frac{\partial \bar{u}}{\partial z} = -\frac{\partial \overline{u'v'}}{\partial y} - \frac{\partial \overline{u'w'}}{\partial z} - \frac{d\bar{p}}{dx} + \frac{1}{Re_\tau} \nabla_{yz}^2 \bar{u}. \quad (7)$$

In this non-dimensional equation, u_τ and D are used as the velocity and length scales respectively. Equation (7) applies to a fully developed turbulent flow and is averaged

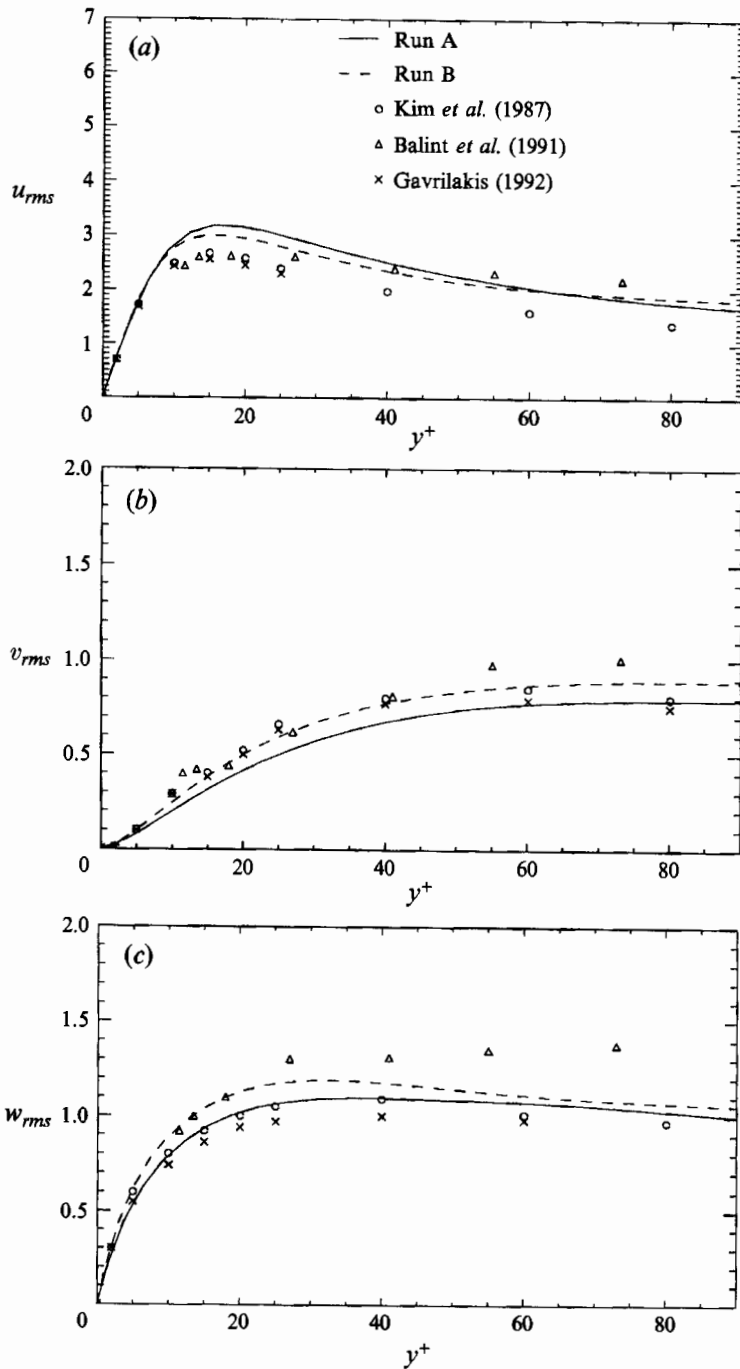


FIGURE 8. Comparison of r.m.s. fluctuations along the wall bisector normalized by the local friction velocity: (a) u_{rms} ; (b) v_{rms} ; (c) w_{rms} .

in both the homogeneous x -direction and in time. Consequently, all the x - and t -derivatives vanish except for $d\bar{p}/dx$, which is the constant driving pressure gradient. The terms in the \bar{u} -equation, (7), are plotted in figure 9(a-c) at different locations. All the budget-terms were calculated directly as they appear in (7) in which the convection

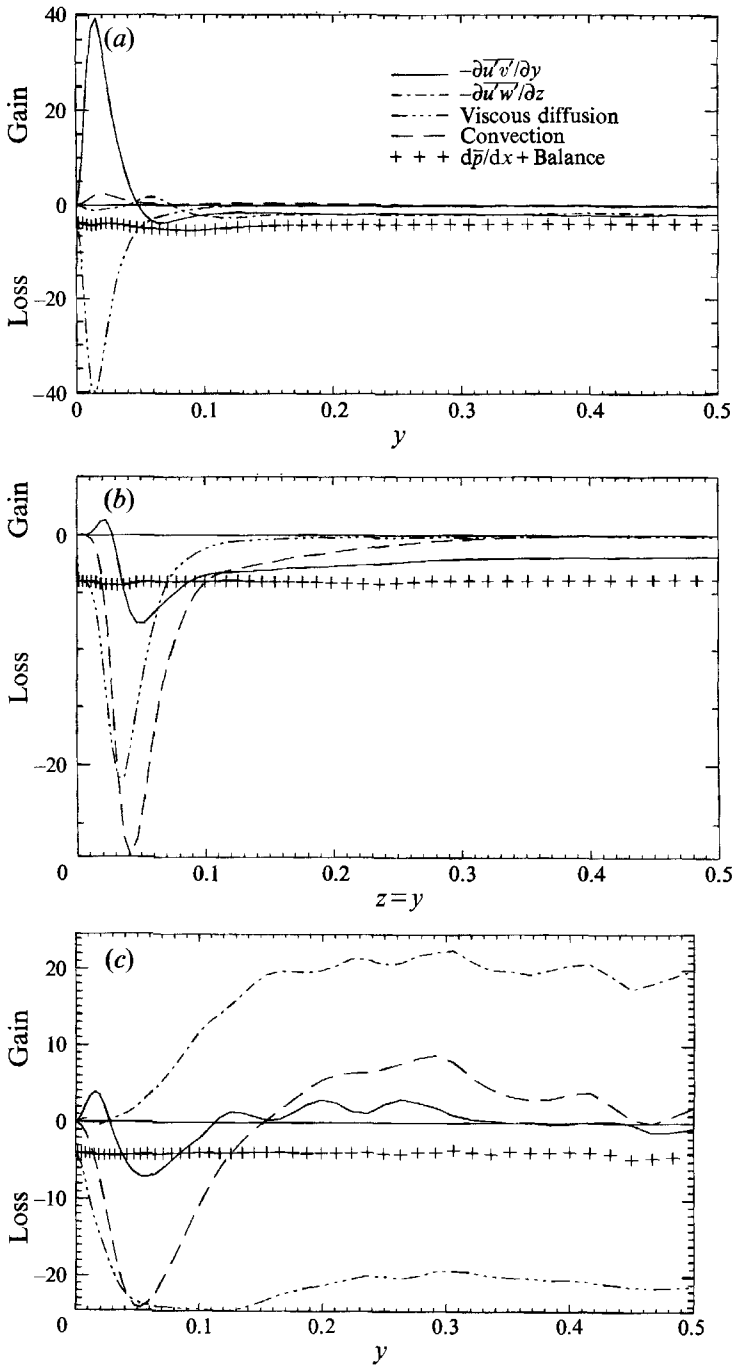


FIGURE 9. Ensemble-averaged \bar{u} -budget distribution at different locations; (a) wall bisector, $z = 0.5$; (b) corner bisector, $z = y$; (c) $z = 0.027$.

terms (the left-hand side) balance all the other terms. Along the wall bisector (figure 9a) for $y > 0.2$, the sum of the primary Reynolds shear stress gradients (the two first terms on the right-hand side of (7)) balances the pressure gradient, and the contribution from convection in figure 9(a) is small. The low convection along the wall bisector is

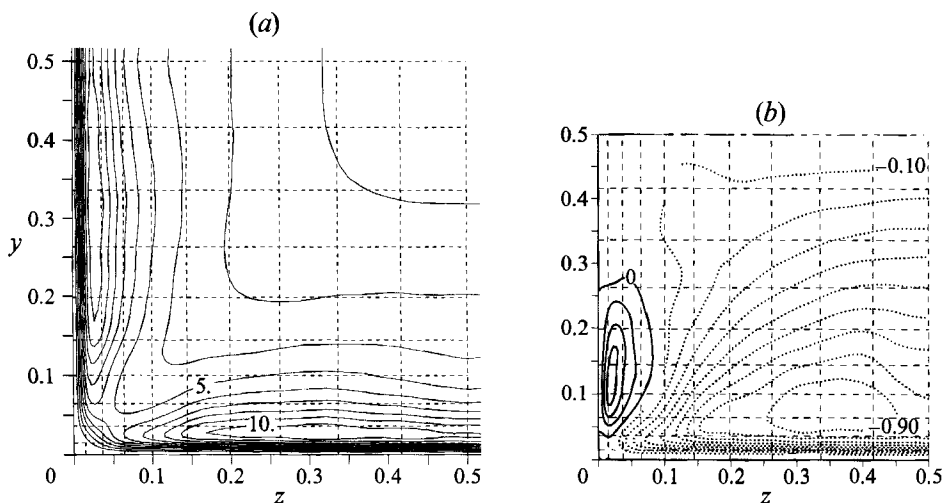


FIGURE 10. Primary Reynolds stress contours in the lower left quadrant of the transverse plane from Run B; every fifth grid-line is dashed: (a) $\overline{u'^2}$ -contours, increment = 1.0; (b) $\overline{u'v'}$ -contours, increment = 0.1.

associated with the low-Reynolds-number effect (see figure 7a) which is characterized by a relatively weak \bar{v} -velocity in this region.

The contour plots in figure 10 and the distributions in figure 11 delineate how the primary Reynolds stresses are influenced by the corner. The primary normal stress ($\overline{u'^2}$) is significantly reduced in the regions near the corner bisector (figures 10a and 11c), consistent with the reduced \bar{u} -gradient here (see figure 4a). Also, considering the horizontal wall, the peak value of $\overline{u'^2}$ is at $z \approx 0.31$, and not at $z = 0.5$, as in the high-Reynolds-number experiment of Brundrett & Baines (1964). This is a low-Reynolds-number effect related to the reduced \bar{v} -velocity at the wall bisector. The contour plots of $\overline{u'v'}$ display asymmetric behaviour (figure 10b), where the reduced $|\overline{u'v'}|$ at the wall bisector ($z = 0.5$) compared to its value at $z = 0.35$ is a manifestation of the low-Reynolds-number effect. The shear stress, $\overline{u'v'}$, increases and reaches a maximum value near the vertical wall when this is approached horizontally from $z = 0.5$ for $0.03 < y < 0.3$. The positive $\overline{u'v'}$ at the vertical wall (also illustrated on figure 11b) is probably associated with bursting events from this wall and with the organization of the ejection structures near the corner; this issue is investigated further in §5. The distributions of $\overline{u'w'}$ (figure 11b) are similar to the distributions of $\overline{u'v'}$ so that $\overline{u'w'}(y) = \overline{u'v'}(z)$. A contour plot of $\overline{u'w'}$ is therefore obtained by a 90° rotation of the $\overline{u'v'}$ -contour plot in the (y, z) -plane.

Toward the corner where the secondary velocities are stronger, mean convection becomes significant. Figure 9(b) indicates that near the corner, along the corner bisector, mean convection balances both the viscous diffusion (the last term on the right-hand side of (7)) and the turbulent shear stress gradients. This negative convection represents a loss in the \bar{u} -momentum equation, with a minimum value at $y = z = 0.04$ (figure 9b). The same effect was also found by Gessner (1973) who investigated the total kinetic energy equation. Accordingly, the positive primary shear stress gradient along the corner bisector causes energy loss, which is compensated by momentum gain due to mean convection.

The viscous diffusion of \bar{u} is reduced along the corner bisector due to the reduced \bar{u} -gradients but it is still significant (figure 9b). In the vicinity of the corner, the turbulent

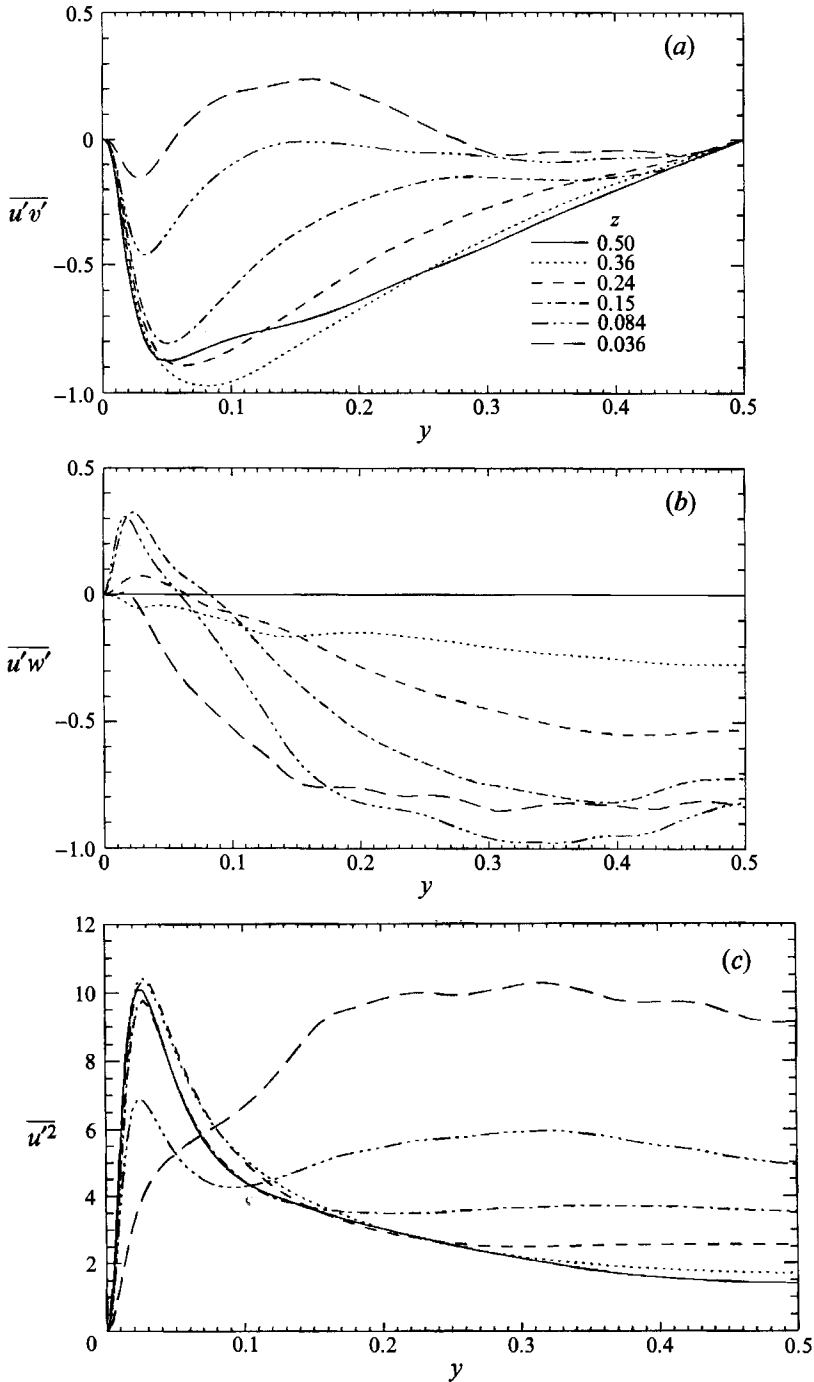


FIGURE 11. Primary Reynolds stress distribution at different z -locations: (a) $\overline{u'v'}$; (b) $\overline{u'w'}$; (c) $\overline{u'^2}$.

shear stress gradients generally contribute to momentum loss in the \bar{u} -budget (figure 9b) as opposed to momentum gain caused by $-\partial\overline{u'v'}/\partial y$ at the wall bisector (figure 9a). The resulting negative convection is also observed along the vertical wall near the corner (figure 9c) generated by a faster decrease in $-\partial\overline{u'w'}/\partial z$ than the increase of the

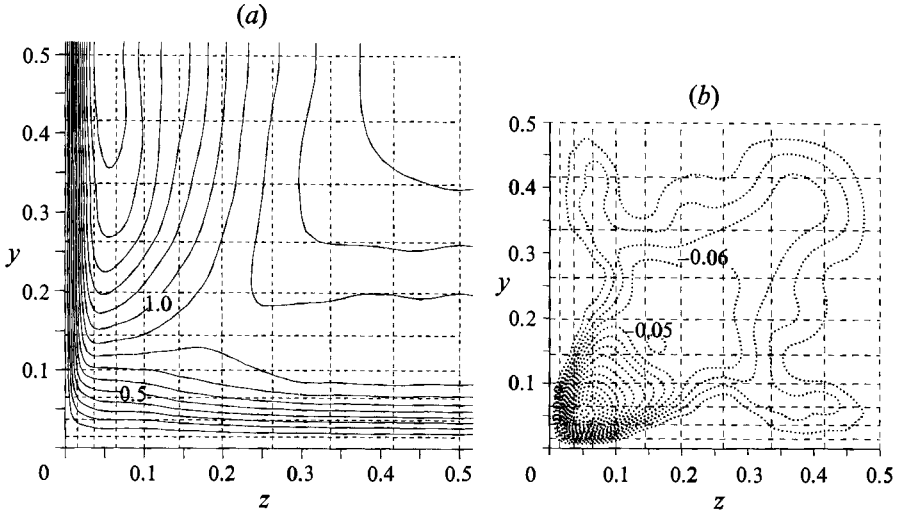


FIGURE 12. Secondary Reynolds stress contours in the lower left quadrant of the transverse plane from Run B: (a) v'^2 -contours, increment = 0.1; (b) $v'w'$ -contours, increment = 0.01.

viscous diffusion term toward the horizontal wall. Along the vertical wall for $y > 0.15$, reduced viscous effects and increased shear stress gradients cause positive convection in this region (figure 9c), which in turn, reduces the streamwise momentum. It is interesting to note that, according to figure 10(a), the turbulence level attains a maximum value in these positive \bar{u} -convection regions, despite the reduced \bar{u} -shear. The maximum \bar{u}'^2 at this location is caused by the relatively high turbulent primary shear stress. The turbulence production is proportional to both the mean velocity shear and the turbulent shear stresses. The maximum primary shear stress occurs where the convection is highest, and *not* at the location where the maximum \bar{u} -shear occurs. This suggests that in addition to the mean shear, $\partial\bar{u}/\partial y$, the mean convection, $\bar{v}\partial\bar{u}/\partial y$, should be accounted for in turbulent shear stress closure models.

In summary, the inhomogeneous distribution of turbulence production via the primary turbulent shear stresses instigates convection of the \bar{u} -velocity, distorting the isotachs, as first explained by Prandtl (1952).

4.4. Mean streamwise vorticity equation

The mean streamwise vorticity equation is obtained by eliminating pressure from the mean secondary flow momentum equations and substituting the mean streamwise vorticity, $\bar{\omega}_x = \partial\bar{w}/\partial y - \partial\bar{v}/\partial z$; this equation reads (Perkins 1970)

$$\bar{v}\frac{\partial\bar{\omega}_x}{\partial y} + \bar{w}\frac{\partial\bar{\omega}_x}{\partial z} = \frac{\partial^2}{\partial y\partial z}(\overline{v'^2} - \overline{w'^2}) + \left(\frac{\partial^2}{\partial z^2} - \frac{\partial^2}{\partial y^2}\right)\overline{v'w'} + \frac{1}{Re_\tau}\nabla^2\bar{\omega}_x. \quad (8)$$

Equation (8) demonstrates the importance of the secondary Reynolds stresses to the mean streamwise vorticity production, and the estimation of these terms has been the subject of several investigations (Brundrett & Baines 1964; Gessner & Jones 1965; Perkins 1970; Madabushi & Vanka 1991; and Gavrilakis 1992). Gessner & Jones (1965) first found that both secondary Reynolds stress terms (the first two terms on the right-hand side of (8)) contribute to the production of secondary flow. This was also confirmed by Perkins (1970), who argued that the secondary flow is generated by the difference between the secondary normal stresses ($\overline{v'^2} - \overline{w'^2}$), and that the secondary shear stress term, $(\partial^2/\partial z^2 - \partial^2/\partial y^2)\overline{v'w'}$, acts like a transport term in (8).

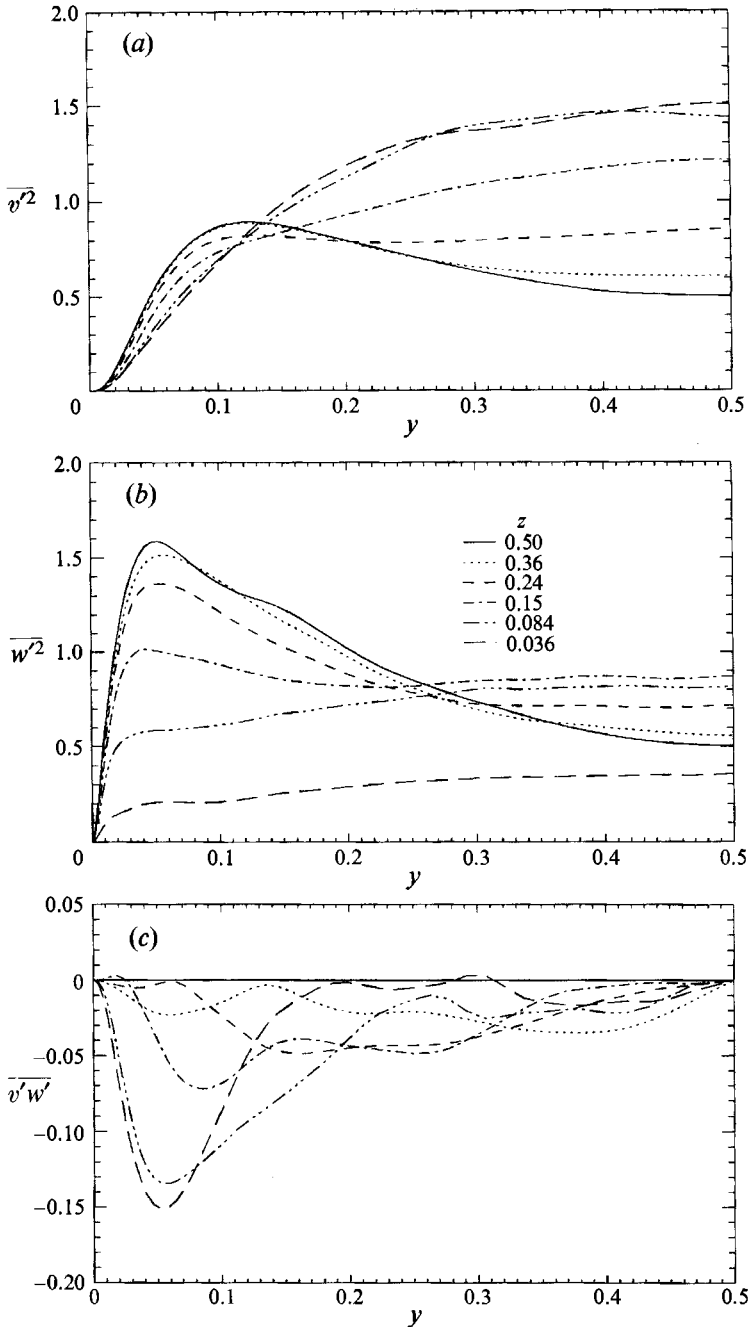


FIGURE 13. Secondary Reynolds stress distribution at different z -locations: (a) $\overline{v'^2}$; (b) $\overline{w'^2}$; (c) $\overline{v'w'}$.

Contour plots and y -distributions of the secondary normal stress, $\overline{v'^2}$ (figures 12a and 13a), display asymmetric behaviour. Owing to the greater damping effect of the horizontal wall, $\overline{v'^2}$ has a lower value here than the near vertical wall. Because of flow-field symmetry, the $\overline{w'^2}$ -distribution is obtained by a 90° rotation of the $\overline{v'^2}$ -distribution (figure 13b). Note that the y -gradient of $\overline{v'^2}$ near the corner for $y < 0.1$ is significantly

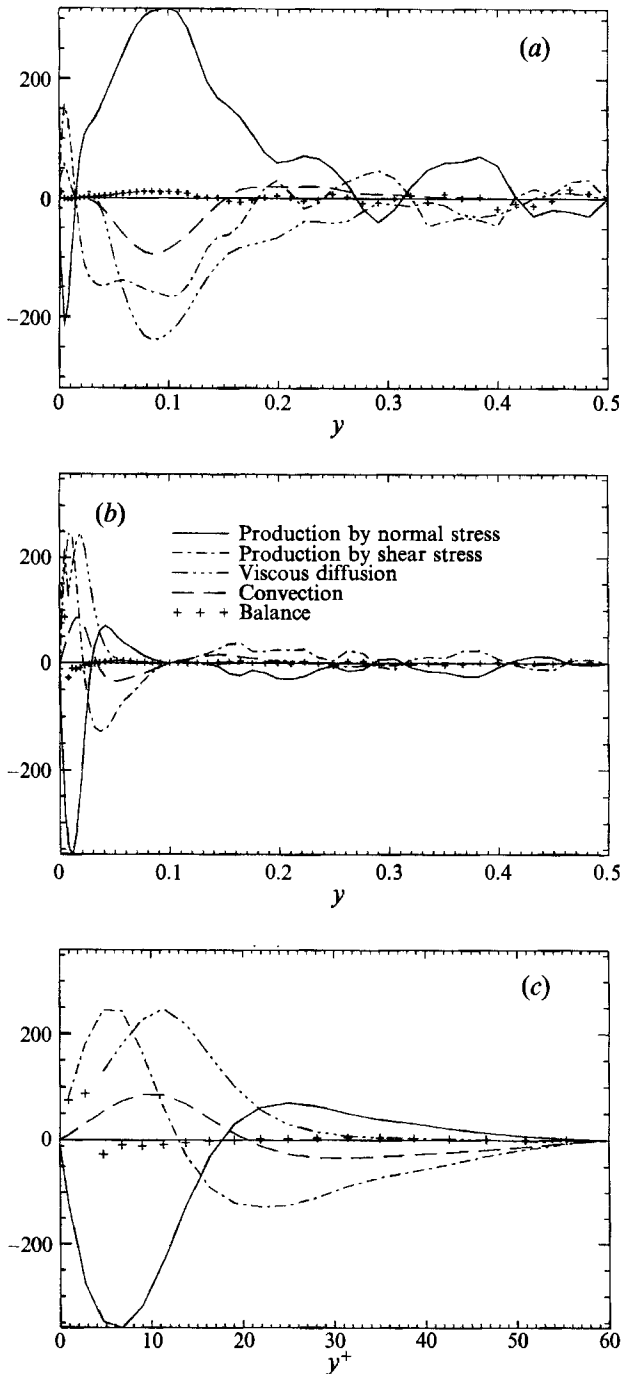


FIGURE 14. Ensemble-averaged \bar{w}_x -budget distribution at two z -locations: (a) $z = 0.015$; (b) $z = 0.1$; (c) $z = 0.1$ plotted versus y^+ coordinates.

reduced compared to the gradient along the wall bisector (see figure 13a). This illustrates one of the secondary effects which produce the secondary flow, and can be explained by an energy transfer from the v'^2 -component to the w'^2 -component (opposite above the corner bisector). More detail on the characteristics of this energy

transfer process is provided in §7. Contours and distributions of the secondary shear stress, $\overline{v'w'}$, in the (y, z) -plane are presented in figure 12(b) and 13(c), and display a significant minimum value near the corner.

The y -distributions of the four terms in (8) are plotted in figure 14(a–c) for two z -locations. The balance, denoted by a + at each grid point, indicates small deviations from zero except for the two grid points near the wall (see figure 14c). This error is due to the calculation of the viscous diffusion term during post-processing, which involves the use of one-sided finite differences at the wall for the calculation of third-order derivatives of the velocity field. At $z = 0.1$ the distributions reach peak values near the wall where the maximum production of streamwise vorticity takes place (Madabushi & Vanka 1991 and Gavrilakis 1992). Figure 14(a) presents the distribution of these terms near the vertical wall at $z = 0.015$; the convection has a minimum at $y \approx 0.09$ where the vorticity is negative. Normal stress gradients decrease the magnitude of the vorticity here in agreement with the results of Gavrilakis (1992). Figure 14(b, c) demonstrates how the negative vorticity is produced *below* the corner bisector: near the wall for $y^+ < 18$ (figure 14c) negative vorticity is produced by the secondary normal stress and for $y^+ > 18$ negative streamwise vorticity is produced by the secondary shear stress by transporting it outward from the wall.

Near the horizontal wall $\overline{\omega}_x$ is positive owing to the no-slip boundary conditions; this is caused by strong positive viscous diffusion together with the positive shear stress gradient ($y^+ < 20$ in figure 14c). As noted by Gavrilakis (1992) this indicates the importance of the viscous diffusion, which was assumed to be negligible by Demuren & Rodi (1984).

5. Quadrant analysis

In the previous section, it was shown how the anisotropic Reynolds stresses were responsible for the convection of streamwise velocity and vorticity. In this section, quadrant analysis is used to describe the mechanisms which create the off-diagonal Reynolds stresses ($\overline{u'v'}$, $\overline{u'w'}$ and $\overline{v'w'}$). By connecting specific turbulence structures to the generation of the anisotropic Reynolds stresses, we intend to provide a physical understanding of the generation of secondary flow of the second kind.

Quadrant analysis generally provides information about the total turbulence production from various events which occur in a turbulent flow (Kim *et al.* 1987) by dividing the Reynolds shear stress into four categories according to the signs of the fluctuating velocities (figure 15). In this analysis, for the square duct, positive v' - and w' -velocities always point away from the *nearest* wall in the y - and z -directions, respectively. In wall-bounded turbulent flows, Q2 and Q4 events for the primary shear stress, $-\overline{u'v'}$, are associated with low-speed ejections and high-speed sweeps, respectively. The other events are not associated with any particular turbulence structure when there is only one inhomogeneous direction. In the present flow, because there are two inhomogeneous directions, the Q1 and Q3 events are also associated with turbulence structures as are the Q2 and Q4 events. Note that in the present flow, Q1–Q4 events describe the creation of both $\overline{u'v'}$ and $\overline{u'w'}$ which act in the y - and z -directions, respectively whereas the Q1_s–Q4_s events are related to the generation of secondary shear stress ($\overline{v'w'}$). In the subsequent analysis, results from Run B are ensemble averaged and presented for the lower left quadrant of the duct.

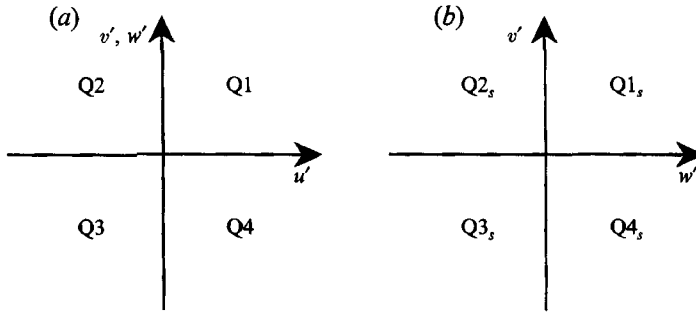


FIGURE 15. Categorizing Reynolds shear stress events in quadrant analysis: (a) $\overline{u'v'}$ and $\overline{u'w'}$; (b) $\overline{v'w'}$.

5.1. Primary shear stress correlations

In this section, quadrant analysis is employed to identify the contribution from the ejection and sweep events to the production of $\overline{u'v'}$ and $\overline{u'w'}$ correlations. Instantaneous pictures of the ejection structure, discussed in the next section, illustrate two counter-rotating streamwise vortices existing in the shear layer near the wall, with the rotational directions pointing upward from the wall between the vortices. This forces low-momentum fluid at the wall to enter the high-speed core of the flow, and the flow between the vortices is a Q2 event with negative u' and positive v' . The sweeps, which are more difficult to visualize because they are not directly associated with streamwise vortices, are associated with an inrush of high-momentum fluid towards the wall region and are Q4 events with positive u' and negative v' . The time evolution of a burst event was schematically described by Lumley (1991) by a proper orthogonal decomposition (POD) analysis of the near-wall region analysing the effect of the bursts on streamwise vortices. The burst event occurs in an aperiodic manner where one cycle starts with two counter-rotating vortices which suddenly increase the updraft between them, ejecting low-momentum fluid into the high-speed core of the flow. The vortices further drift apart and a gentle downdraft occurs between them, recognized as a sweep. The cycle continues with the start of two new ejections, one on each side of the old one, shifted one burst period in the spanwise direction. One burst period occupies one streamwise vortex and was found to be around $\Delta z^+ = 100$ using wall coordinates, where wall coordinates are given by $z^+ = zRe_\tau$ (Kline *et al.* 1967).

In the square duct, it is reasonable to assume that the same turbulence structures are present as in channel flow, and the average deviation of these structures (from channel flow characteristics) creates the turbulence characteristics of the secondary flow; these deviations are largest in the corners where the anisotropies are largest.

In figure 16(a) and 16(b), the contribution of Q-events to the total $\overline{u'v'}$ -distribution (along y) is presented at two z -locations, $z = 0.5$ and 0.135 . A comparison of these figures reveals that Q3 events are most influenced by the corner effects. The Q3 events are created by the correlation between $-u'$ and $-v'$, so that the ejection event is responsible for this correlation because of the negative u' . The strength of Q3 events increases when going from the wall bisector towards the vertical wall. Consequently, these events must be created by ejections from the vertical wall, resulting in the increase of $\overline{u'v'}$ in this region.

In the previous section we showed that the mean convection of the streamwise velocity was created by both the $\overline{u'v'}$ and the $\overline{u'w'}$ -stresses. The $\overline{u'w'}$ -correlation is zero in channel flow owing to the homogeneous z -direction, but in the present flow the

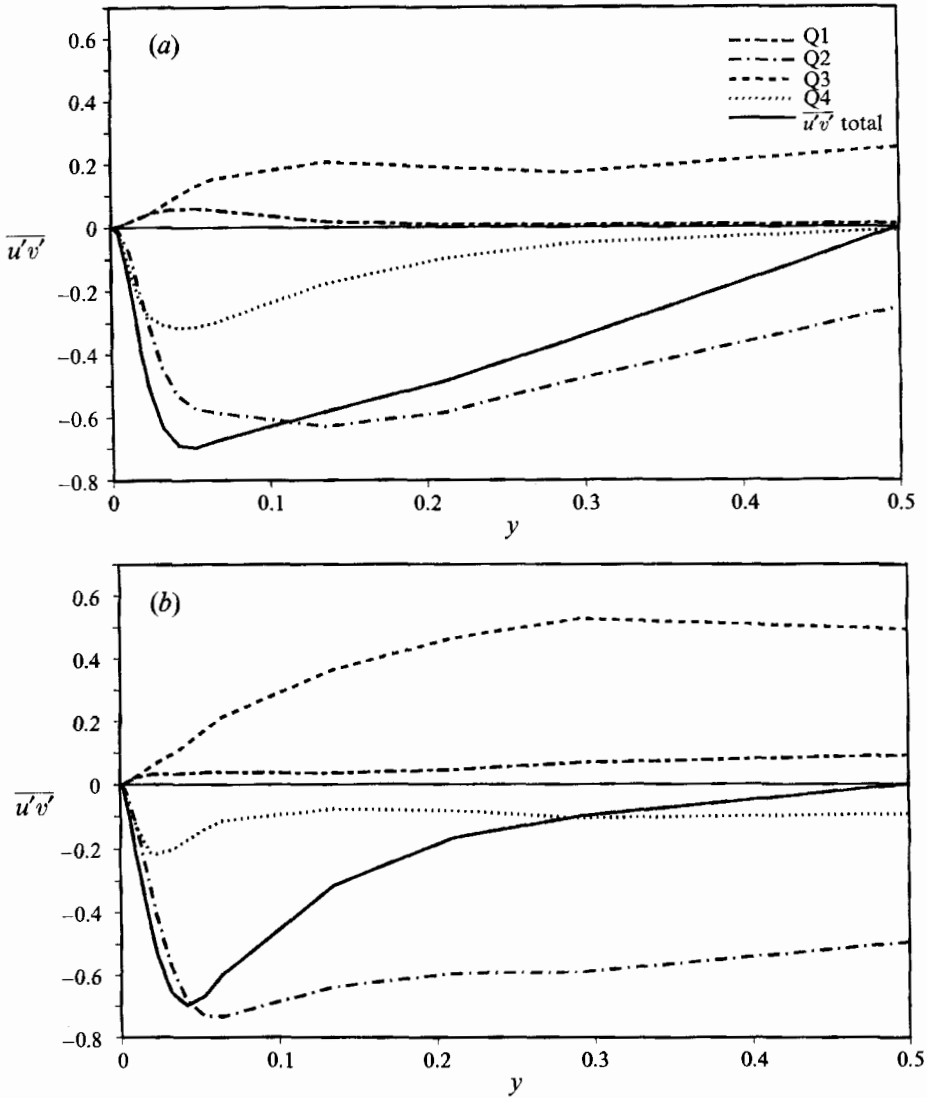


FIGURE 16. Reynolds shear stress, $\overline{u'v'}$, from each quadrant as a function of y ;
(a) $z = 0.5$; (b) $z = 0.135$.

behaviour of $\overline{u'w'}$ becomes important. Contribution from the different quadrants to $\overline{u'w'}$ -production above the horizontal wall is illustrated in figure 17. The ejection events (Q2 and Q3) in figure 17 represent the upper part of an ejection structure, where Q2 belongs to the right eddy and Q3 belongs to the left eddy (looking downstream). At the wall bisector (figure 17a), each quadrant contributes significantly to this stress component, but the sum is zero; we will refer to this effect as 'the cancelling effect'. Toward the vertical wall where deviation from the homogeneity in the z -direction becomes important, figure 17(b) depicts the Q-events which contribute to the total $\overline{u'w'}$ -stress. Accordingly, close to the horizontal wall $\overline{u'w'}$ is positive, created by strong Q1 and Q3 events; also, further away from the wall, negative $\overline{u'w'}$ is primarily created by Q2 events. Close to the corner below the corner bisector, both streaks and ejections contribute to positive $\overline{u'w'}$. The contribution from ejections create positive $\overline{u'w'}$ because

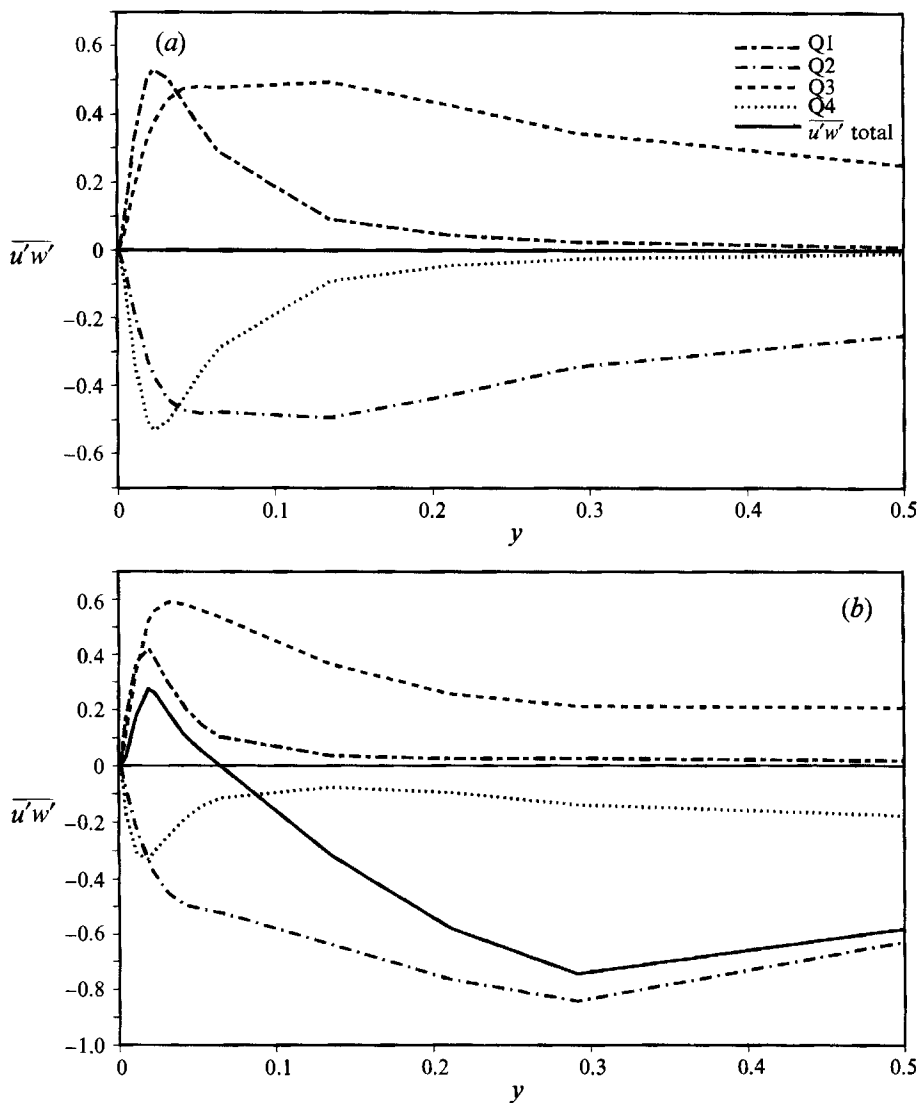


FIGURE 17. Reynolds shear stress, $\overline{u'w'}$, from each quadrant as a function of y ; (a) $z = 0.5$; (b) $z = 0.135$.

Q3 events are stronger than Q2 events, and this suggests that the ejections from the horizontal wall on average bend toward the vertical wall. This difference between Q2 and Q3 events can also be explained by the average location of the first ejection from the horizontal wall measured from the origin; the left streamwise vortex in this ejection rotates counterclockwise, so that the Q3 events dominate the Q2 events.

Owing to its direct connection to the mean streamwise momentum equation, the distribution of $\overline{u'w'}$ as a function of z above the horizontal wall is perhaps the most useful quantity to describe the convection of streamwise velocity. In figure 18(a) the Q-events contributing to the total $\overline{u'w'}$ -correlation are plotted as a function of z at $y = 0.042$. From the total $\overline{u'w'}$ (figure 18a, solid line) the z -gradient of $-\overline{u'w'}$ is found to be positive for $0 < y < 0.02$, negative for $0.02 < y < 0.14$ and positive for $0.14 < y < 0.3$ (see the budget distributions in figure 9c). At this cross-section close to

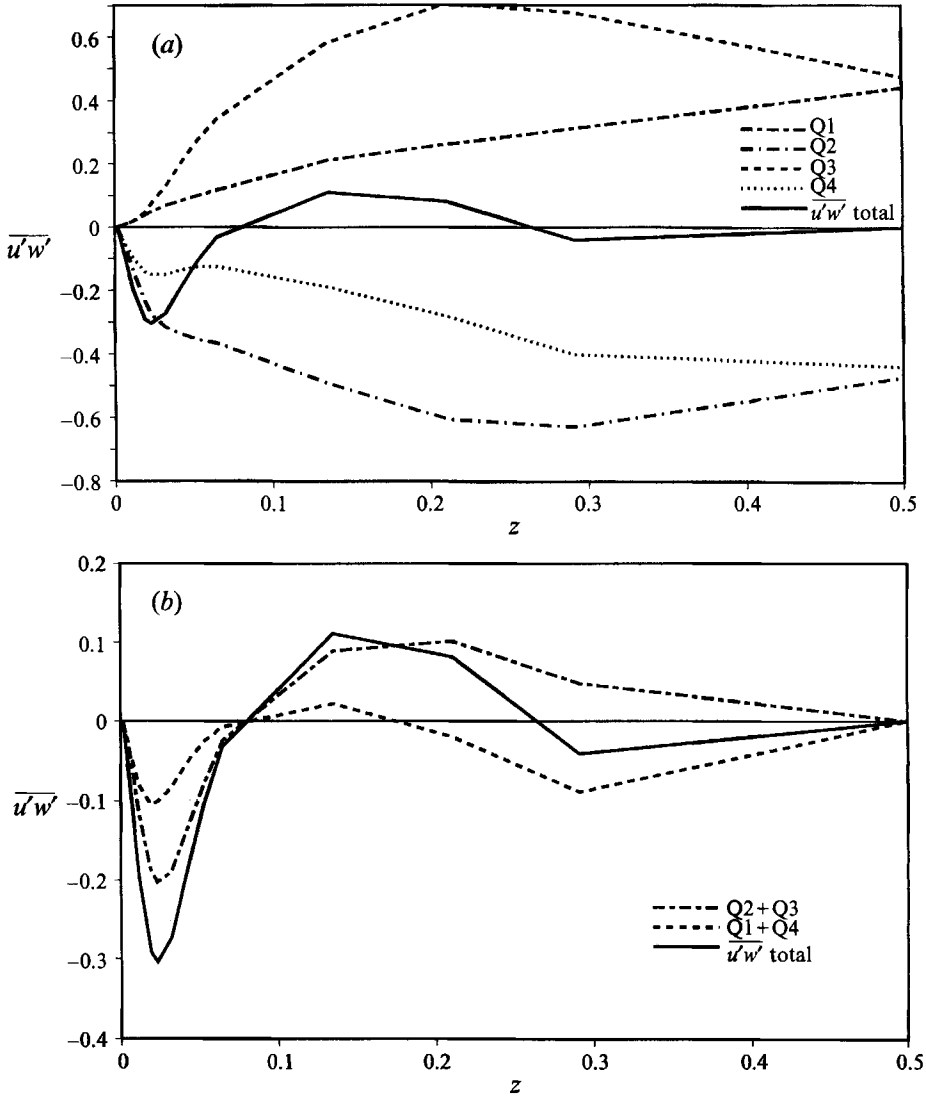


FIGURE 18. Reynolds shear stress, $\overline{u'w'}$, from each quadrant as a function of z at $y = 0.042$; (a) all $\overline{u'w'}$ quadrant events; (b) comparing contribution from sweeps (Q1 + Q4) and ejections (Q2 + Q3).

the corner, typically the ejection event dominates the streak event in the production of $\overline{u'w'}$ (figure 18 b); the total contribution to the $\overline{u'w'}$ -correlation from the sum of Q2 and Q3 events is generally twice the contribution from the sum of Q1 and Q4. It is noted that the contributions from the individual quadrant events creating $\overline{u'w'}$ above the horizontal wall are comparable in magnitude to the quadrant events creating $\overline{u'v'}$, but owing to the cancelling effect of the $\overline{u'w'}$ -events, their sum is reduced; $\max|\overline{u'w'}|$ is about 40% of $\max|\overline{u'v'}|$.

In summary, the positive $\overline{u'w'}$ above the horizontal wall with a maximum between $(y, z) = (0.025, 0.1)$ and $(0.025, 0.2)$ is caused primarily by ejections from this wall. Two related effects contribute to this phenomenon. Because there can be no ejections from the corner, the first ejection from the horizontal wall near the corner will ensure that Q3 events will be dominant. Also, the interactions between ejections from both walls

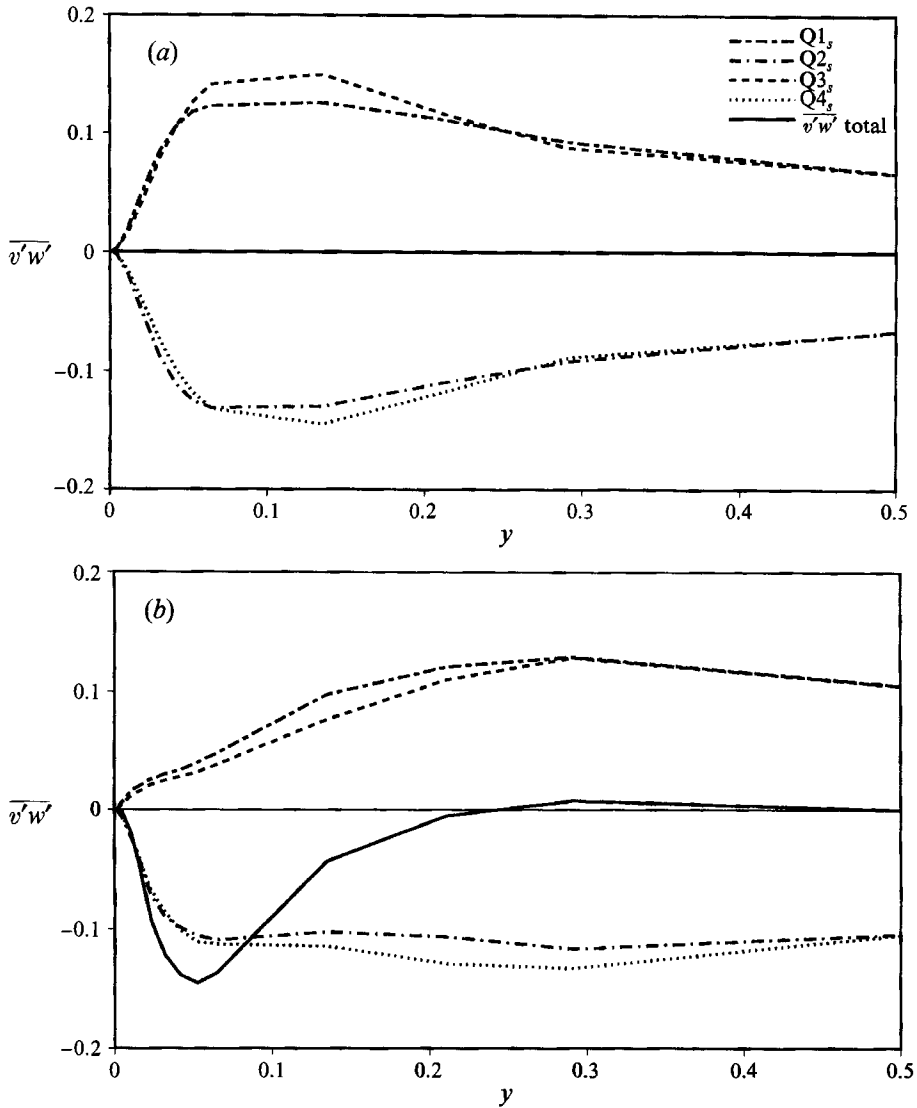


FIGURE 19. Reynolds shear stress, $\overline{v'w'}$, from each quadrant as a function of y ;
(a) $z = 0.5$; (b) $z = 0.042$.

will bend the ejection stem toward the perpendicular wall, creating Q3 events. In §6, instantaneous flow field structures will be presented in order to further illustrate the second effect.

5.2. Secondary shear stress correlation

In this section, the quadrant analysis is extended to the secondary shear stress, $\overline{v'w'}$. The importance of this quantity lies in the fact that together with the difference between the secondary normal stresses ($\overline{v'^2} - \overline{w'^2}$) it contributes to the production and transport of mean streamwise vorticity.

Contributions to the secondary stress from the individual Q-events are also significant when there is only one inhomogeneous direction, but for such flows the sum is zero (the cancelling effect). Figure 19(a) illustrates the Q-event contributions to the secondary shear stress at the wall bisector in the square duct flow. The turbulence

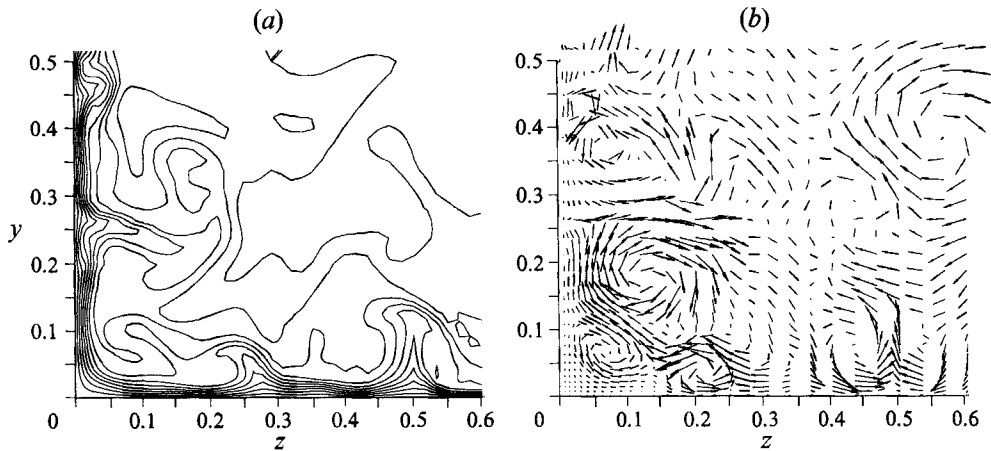


FIGURE 20. Instantaneous velocity, pressure, and streamwise vorticity distributions in the transverse plane: (a) U/u_s -contours, increment = 2; (b) v, w velocity vectors.

events creating the $\overline{v'w'}$ -shear stress are most likely to be associated streamwise vortices; $Q1_s$ and $Q2_s$ events are created by secondary flows directed up from the wall with an angle in either the right or left direction (looking downstream), respectively, and the $Q3_s$ and $Q4_s$ events are similarly created by the downward motion towards the wall. These streamwise vortices are created by ejections, and owing to the lack of ejections from the corner (origin), turbulence fluctuations in the corner bisector direction are reduced. Figure 19(b) shows that the turbulence fluctuations perpendicular to the corner bisector (represented by $Q2_s$ and $Q4_s$ events) are maintained until around $z = 0.05$ when the corner is approached from the wall bisector at $z = 0.5$, whereas the contribution of the $Q1_s$ and $Q3_s$ events start to decrease at around $z = 0.3$. The reason why the $Q2_s$ contribution is maintained closer to the corner (figure 19b) may also be due to the interaction between ejections from both walls tilting the ejection stem toward the perpendicular wall. The combined effect of no ejections from the corner and the tilted ejection stems causes the $Q2_s$ and $Q4_s$ events to be stronger than the $Q1_s$ and $Q3_s$ events, resulting in a negative $\overline{v'w'}$ -correlation.

This analysis indicates that the magnitude of the $\overline{v'w'}$ -correlation is significant in the corner region and is about 20% of the maximum primary shear stress ($|u'v'|$).

6. Instantaneous flow structures

In this section we present an illustrative cross-section of the instantaneous turbulence structures which contribute to the production of shear stresses.

We consider the instantaneous streamwise velocity contours and secondary velocity vectors at a cross-section in the (y, z) -plane (figure 20). First we examine an ejection which is not influenced by the sidewalls which appears at $z = 0.5$ near the horizontal wall; the characteristic mushroom-like shape is depicted in figure 20(a) and two counter-rotating vortices exist at the same place in figure 20(b).

Near the corner, several ejections can be observed. The strongest ejection, whose mushroom shape is evident in figure 20(a), starts from the vertical wall at around $y = 0.25$. The velocity vectors display two counter-rotating vortices, one below and one above this ejection structure. The lower vortex is most pronounced, and it appears that this vortex interacts with another ejection structure from the horizontal wall. Figure

20(a) indicates that an ejection event is starting at around $z = 0.25$ from the horizontal wall, and the stem of this ejection stretches out toward the vertical wall and joins the lower vortex belonging to the stronger ejection from the vertical wall.

It must be emphasized that these instantaneous pictures only serve as an example of typical turbulence structures in this flow which are responsible for the interactions between ejections from both walls; this interaction results in the bending of the ejection stems.

7. Pressure–velocity correlations

In second-order turbulence closures, modelling of the pressure–velocity correlations is the key to a successful model. In this section, we investigate the behaviour of the pressure–velocity correlations as they relate to the production of secondary flow and to the distortion of the isotachs.

The influence of pressure fluctuations on the Reynolds stress transport equations is contained in the velocity–pressure gradient correlation,

$$\Pi_{ij} = -\overline{u'_i \frac{\partial p'}{\partial x_j}} - \overline{u'_j \frac{\partial p'}{\partial x_i}}. \quad (9)$$

In turbulence models, Π_{ij} is usually split into a pressure–strain correlation and a pressure–diffusion correlation (by the chain rule):

$$\Pi_{ij} = \Phi_{ij} + T_{ij}^P, \quad (10)$$

and each term is written

$$\Phi_{ij} = 2\overline{p' s'_{ij}} \quad \text{pressure–strain}, \quad (11)$$

$$T_{ij}^P = -\frac{\partial}{\partial x_k} (\overline{p' u'_i \delta_{jk}} + \overline{p' u'_j \delta_{ik}}) \quad \text{pressure–diffusion}, \quad (12)$$

where $s'_{ij} = \frac{1}{2}(\partial u_j / \partial x_i + \partial u_i / \partial x_j)$ is the fluctuating strain rate, and δ_{ij} is the Kronecker delta.

7.1. Diagonal pressure–strain terms

The reduced $\overline{v'^2}$ gradient, $\partial \overline{v'^2} / \partial y$, near the corner along the horizontal wall (see figure 12a), which becomes an important contributor to the source of the streamwise vorticity (equation (8)) can be explained by the redistribution of $\overline{v'^2}$ -energy to $\overline{w'^2}$ -energy through the pressure–strain (or velocity–pressure gradient) correlations. This effect is similar to the ‘splating’ effect that occurs in the vicinity of a solid boundary (Moin & Kim 1982). The difference between the ‘splating’ effect and this ‘corner’ effect can be observed in figure 21(a, b) in which the diagonal terms in the pressure–strain tensor are plotted as a function of y at two z -locations: in the first location both the corner and the splating effects are present and in the other location only the splating effect is present. Near the corner, where both effects coexist, at $z = 0.064$ (figure 21a), Φ_{22} becomes a loss to the $\overline{v'^2}$ -budget for $y < 0.05$. This loss is distributed only to the $\overline{w'^2}$ -budget for $0.02 < y < 0.05$ constituting the corner effect, even though the strongest contribution to $\overline{w'^2}$ is from the $\overline{u'^2}$ -component through Φ_{11} . The splating effect takes place for $y < 0.02$, where $\overline{v'^2}$ -energy is distributed to both $\overline{u'^2}$ and $\overline{w'^2}$, in figure 21(a). Further away from the corner, where only the splating effect is present (figure 21b), this effect is observed close to the wall for $y < 0.02$ with a negative Φ_{22} , increased Φ_{11} and an increased Φ_{33} . Also, the distributions of Φ_{22} and Φ_{33} cross-over on the corner bisector, indicated by the vertical lines in figure 21; above the corner bisector, energy transfer is from $\overline{w'^2}$ to $\overline{v'^2}$. This corner effect can be explained by the interactions

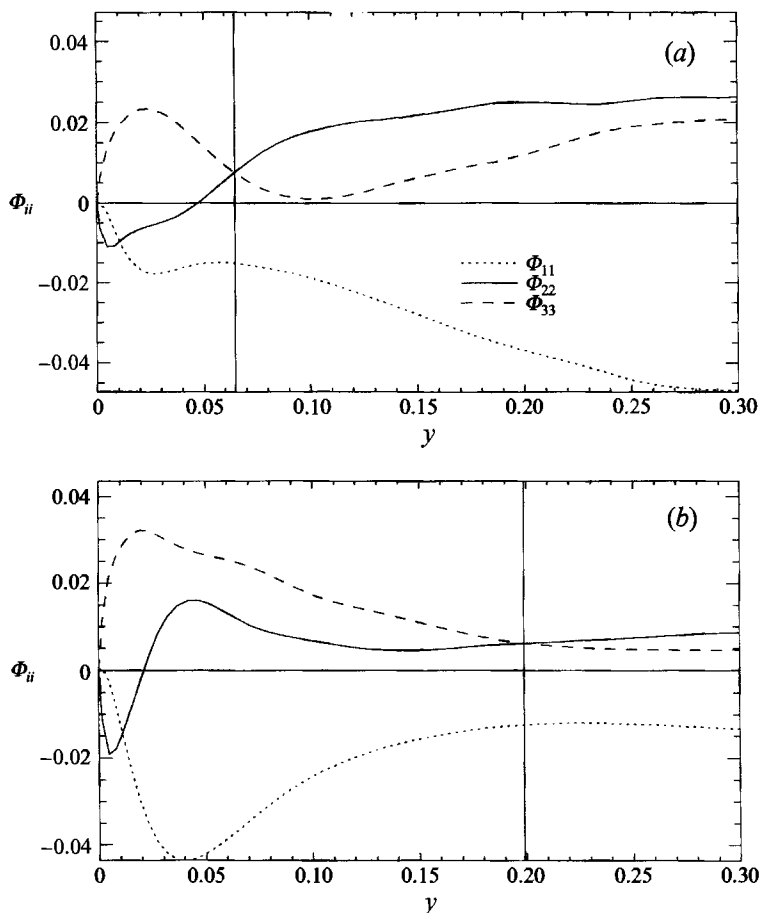


FIGURE 21. Diagonal terms in the pressure-strain tensor at two z -locations : (a) $z = 0.064$;
(b) $z = 0.198$. The vertical line indicates the corner bisector.

between ejections arising from both walls consecutively. The upward motion in an ejection from the horizontal wall is bent toward the vertical wall when an ejection has taken place here. The ejection from the vertical wall will cause a downdraft to the corner caused by the streamwise eddy near the corner. This downdraft will influence the ejection from the horizontal wall and bend its ejection stem toward the vertical wall. Because of this bending, energy is transferred from the v' to the w' -component; in §6, this scenario is illustrated by considering the instantaneous flow field. This interaction of the ejections also results in the $-\overline{v'w'}$ -correlation near the corner. It should be stressed that the underlying reason for the interaction of ejections giving a mean secondary flow is the lack of bursts from the corner, causing the ejections to be 'locked' at locations away from the corner.

7.2. Transport terms

In second-order turbulence closures, the pressure-strain correlation (equation (11)) is usually modelled directly, and the pressure-diffusion term is modelled together with the turbulent transport term,

$$T_{ij} = -\frac{\partial}{\partial x_k} \overline{u'_i u'_j u'_k}. \quad (13)$$

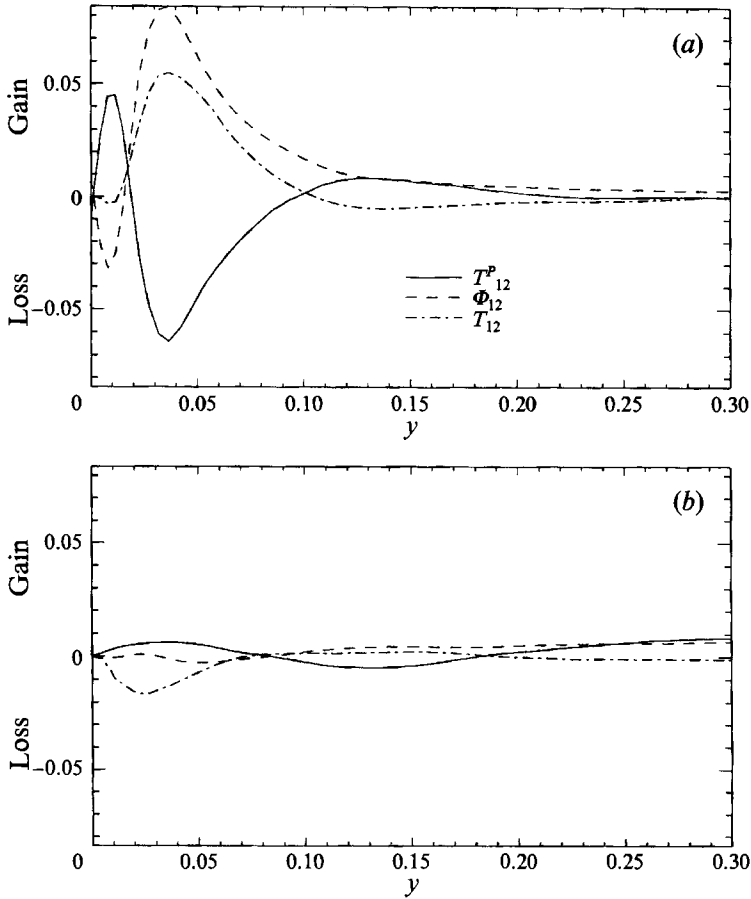


FIGURE 22. Turbulent transport and pressure-velocity terms from the primary shear stress budgets at $z = 0.19$: (a) $\overline{u'v'}$ budget; (b) $\overline{u'w'}$ budget.

However, results from DNS of turbulent channel flow indicate that Π_{ij} , not Φ_{ij} , should be modelled directly because near the wall, Φ_{ij} and the pressure transport term T_{ij}^P are opposite-valued and cancel each other when added (Mansour, Kim & Moin 1988).

Modelling of Π_{ij} may be easier than modelling of Φ_{ij} because the pressure transport term acts differently than the turbulent transport term and lumping them together in a model for $(T_{12} + T_{12}^P)$ will require the model to describe two different effects. For the square duct flow, the two transport terms, T_{12} and T_{12}^P , are plotted in figure 22(a) indicating that the differences are indeed quite significant; T_{12} displays the diffusion process which it represents, whereas T_{12}^P acts in the direction opposite to T_{12} . The sum, $\Pi_{12} = T_{12}^P + \Phi_{12}$, acts as a redistributive term, and in fact the main part of the redistributed gain in the $\overline{u'w'}$ budget for $z < 0.2$, below the corner bisector, comes through the pressure transport term, T_{12}^P (for $y < 0.06$ in figure 22b).

7.3. Off-diagonal velocity–pressure gradient correlations

The off-diagonal velocity–pressure gradient correlations contribute strongly to the anisotropic shear stresses (Huser 1992). A complex interaction between the three off-diagonal shear stress terms was found to be a part of the corner effect.

Considering first the effect that also occur in turbulent channel flow, in figure 23 (a,

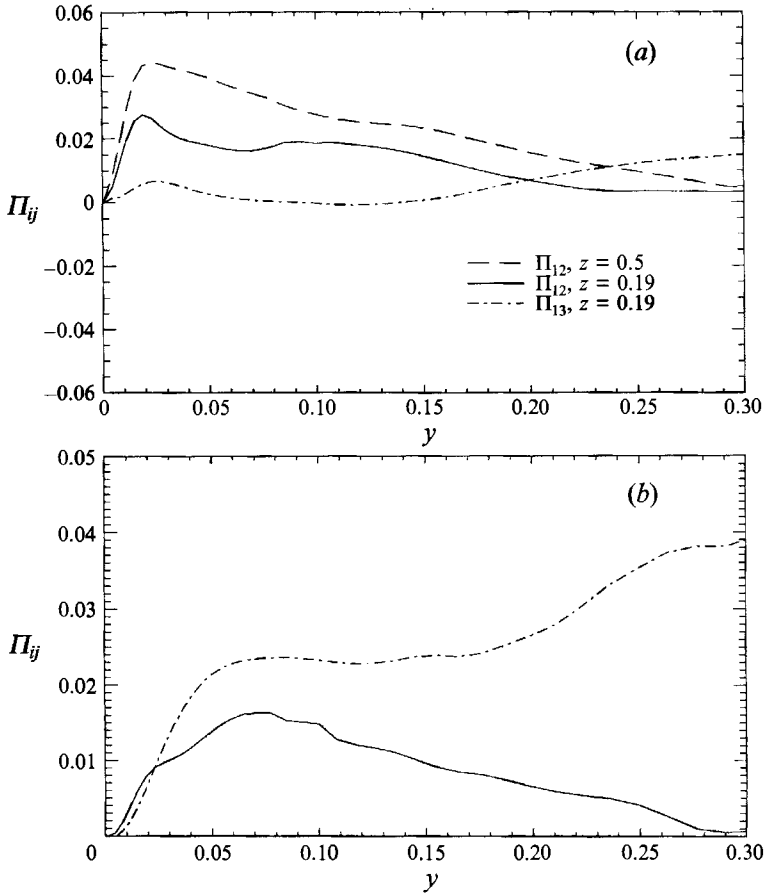


FIGURE 23. Off-diagonal velocity-pressure gradient terms from the primary shear stress budgets: (a) at $z = 0.5$ and $z = 0.19$; (b) at $z = 0.022$.

dashed line) the distribution of Π_{12} at $z = 0.5$ is plotted. This distribution compares well qualitatively with data from Mansour *et al.* (1988), where positive Π_{12} is a loss to the production of $-\overline{u'v'}$. For $z < 0.3$, the effect of the corner becomes pronounced, and the distributions at $z = 0.19$ (figure 23a) indicate that Π_{12} is reduced. The reduction of P_{12} occurs simultaneously with a gain to the $\overline{u'w'}$ -budget through Π_{13} for $y < 0.06$ (figure 23a, chain-dashed line), which is one of the mechanisms by which positive $\overline{u'w'}$ -shear stress is produced (see contour plots of $\overline{u'v'}$, figure 10b. Note that the $\overline{u'w'}$ -contours are obtained from the $\overline{u'v'}$ -contours by rotating $\overline{u'v'}$ 90° in the transverse plane). The connection between $\overline{u'v'}$ - and $\overline{u'w'}$ -stresses can also be observed in the distribution plot of Π_{12} and Π_{13} parallel to the vertical wall at $z = 0.022$ (figure 23b). The reduced Π_{13} along the vertical wall for $z < 0.2$ is probably responsible for the positive Π_{12} at the same location. There is a role reversal for the velocity-pressure gradient terms from the duct centre to the corner; at the duct centre, Π_{12} is positive, but acts as a loss to the negative shear stress ($-\overline{u'v'}$), whereas near the corner, Π_{12} is a gain to the positive shear stress ($\overline{u'v'}$) (figure 23b).

Considering the \bar{u} -momentum budget (§4.3, figure 9c) along the vertical wall, it can be noted that both the reduced magnitude of $\overline{u'w'}$ and the positive $\overline{u'v'}$ create a relative loss to this equation (for $y < 0.2$) through the terms $-\partial\overline{u'w'}/\partial z$ and $-\partial\overline{u'v'}/\partial y$; for $0.05 < y < 0.2$ both the turbulent shear stress terms decrease as the corner is approached

resulting in a decreasing \bar{u} -convection. This reduced \bar{u} -convection becomes negative near the vertical wall. The positive \bar{u} -convection along the vertical (or horizontal) wall, with a maximum value at $y = 0.3$ (see figure 9c), is caused by the large magnitude of $\overline{u'w'}$ combined with a low $\overline{u'v'}$.

Summarizing the off-diagonal pressure-velocity correlation effects in the square duct flow, the present results indicate that negative \bar{u} -convection in the corner is partly created by the velocity-pressure gradient interactions between the two primary shear stresses. This reduction of \bar{u} -convection toward the corner, caused by the redistribution from $\overline{u'v'}$ to $\overline{u'w'}$ via Π_{12} and Π_{13} (below the corner bisector), is similar to the production of streamwise vorticity due to energy transfer from $\overline{v'^2}$ to $\overline{w'^2}$ described in the previous section. This effect is also caused by the arrangement of the primary shear stress production terms; no turbulence model is needed for these terms because they are given by the dependent variables in the governing equations.

8. Conclusions

A new solution procedure for the calculation and analysis of three-dimensional time-dependent incompressible flow in a square duct has been developed. The numerical solution of the Navier-Stokes equations incorporates a projection method and the decoupled equations are solved semi-implicitly by a Runge-Kutta method. Spatial discretization is done by fourth-order central and fifth-order upwind-biased finite differences and by the Fourier pseudo-spectral method.

The present calculations were performed at a Reynolds number $Re_\tau = 600$ (based on the mean friction velocity and the duct width) which is in the fully turbulent regime. At this Reynolds number secondary flows and the isotach distortions are accurately predicted; low-Reynolds-number effects in the simulation are relatively weak and are manifested in the reduction of the secondary flow near the wall bisector compared to high-Reynolds-number experiments. The main secondary effect, which is responsible for the creation of the secondary flows both at high and low Reynolds numbers, is clearly captured in the simulations and is the main topic of the present work.

Turbulence statistics along the wall bisector are computed and compared with data from other wall-bounded turbulent flows, displaying excellent agreement in the viscous sublayer. It is evident from the present results that there is stronger turbulence production along the walls away from the corner compared to channel and boundary-layer flows. This relatively strong turbulence production near the wall bisector combined with the low turbulence production along the corner bisector produce positive and negative convection of the mean streamwise velocity at the respective locations, as evident from the terms in the Reynolds-averaged streamwise velocity equation. Convection of streamwise velocity is responsible for the distorted isotachs and can only occur in the presence of the secondary flows. The terms in the Reynolds-averaged streamwise vorticity equation unveil the mechanism by which the secondary flow is produced by the secondary Reynolds stresses.

An explanation of the mechanisms responsible for the creation of secondary flows of the second kind and the distorted isotachs is offered by considering the dominant turbulence structures in the flow. These (dominant) ejection structures are produced during a bursting event and contain two streamwise counter-rotating vortices. On the horizontal wall the preferred rotational sense of the leftmost streamwise vortex in an ejection that can occur close to the left corner determines the mean rotational sense of the secondary flow in that octant. The reduced mean shear at the corner bisector prohibits ejections from occurring here and thereby allows a mean secondary flow

toward the corner from the core of the duct. The strong ejections along the walls away from the corner promotes a relatively low streamwise velocity compared to the streamwise velocity at the corner bisector, explaining the distorted isotachs.

The characteristic anisotropic Reynolds stress distribution can also be explained by considering the ejection structures and by the 'new' effects that are observed in the vicinity of the corner. Considering the lower left corner of the square duct, the new effects are observed as nonlinear interactions between simultaneous ejections from both walls. These interactions tilt the ejection stems toward the perpendicular wall, creating positive primary shear stress ($\overline{u'v'}$ and $\overline{u'w'}$, above and below the corner bisector, respectively) and negative secondary shear stress ($-\overline{v'w'}$ at the corner bisector). This tilting of the ejection stem also redistributes energy from $\overline{v'^2}$ to $\overline{w'^2}$ (at the horizontal wall in the lower left corner) where v is the vertical and w is the horizontal velocity. This effect is manifested by the behaviour of the pressure-velocity correlation tensor near the corner.

The magnitudes of $\overline{u'w'}$ and $\overline{v'w'}$ reach about 40% and 20%, respectively of the maximum $\overline{u'v'}$ correlation, and the quadrant analysis indicates that the ejection structures contribute most to this anisotropy. Other effects, including sweep events, also contribute, indicating the complexity of the flow.

The authors thank S. Gavrilakis who provided valuable information from his work on square duct flows. The first author acknowledges The Fulbright Foundation, The Norwegian Space Agency and The Royal Norwegian Council for Scientific and Industrial Research (NTNF) for financial support. Cray Research and NCAR are also acknowledged for providing computer time. Partial support for this study was provided by ONR Grant ONR-00014-91-J-1086 with J. A. Fein as the Technical Monitor.

REFERENCES

- ANDERSON, D. A., TENNEHILL, J. C. & PLETCHER, R. H. 1984 *Computational Fluid Mechanics and Heat Transfer*. McGraw-Hill.
- BALINT, J.-L., WALLACE, J. M. & VUKOSLAVČEVIĆ, P. 1991 The velocity and vorticity vector fields of a turbulent boundary layer. Part 2. Statistical properties. *J. Fluid Mech.* **228**, 53.
- BRUNDRETT, E. & BAINES, W. D. 1964 The production and diffusion of vorticity in a square duct. *J. Fluid Mech.* **19**, 375.
- DEMUREN, A. O. 1990 Calculation of turbulence-driven secondary motion in ducts with arbitrary cross-section. *AIAA Paper* 90-0245.
- DEMUREN, A. O. & RODI, W. 1984 Calculation of turbulence-driven secondary motion in non-circular ducts. *J. Fluid Mech.* **140**, 189.
- GAVRILAKIS, S. 1992 Numerical simulation of low Reynolds number turbulent flow through a straight square duct. *J. Fluid Mech.* **244**, 101.
- GESSNER, F. B. 1973 The origin of secondary flow in turbulent flow along a corner. *J. Fluid Mech.* **58**, 1.
- GESSNER, F. B. & EMERY, A. F. 1981 The numerical prediction of developing flow in rectangular ducts. *Trans. ASME I: J. Fluids Engng* **103**, 445.
- GESSNER, F. B. & JONES, J. B. 1965 On some aspects of fully developed turbulent flow in rectangular channels. *J. Fluid Mech.* **23**, 689.
- GESSNER, F. B., PO, J. K. & EMERY, A. F. 1979 Measurement of developing turbulent flow in a square duct. In *Turbulent Shear Flows I*, p. 119. Springer.
- GRESHO, P. M. 1990 On the theory of semi-implicit projection methods for viscous incompressible flow and its implementation via a finite element method that also introduces an early consistent mass matrix. Part 1: Theory. *Intl J. Numer. Meth. Fluids* **11**, 587.

- HARTNETT, J. P., KOH, J. C. Y. & MCCOMAS, S. T. 1962 A comparison of predicted and measured friction factors for turbulent flow through rectangular ducts. *Trans. ASME C: J. Heat Transfer* **84**, 82.
- HUSER, A. 1992 Direct numerical simulation of turbulent flow in a square duct. Doctoral thesis, University of Colorado, Boulder.
- HUSER, A. & BIRINGEN, S. 1992 Calculation of shear-driven cavity flows at high Reynolds numbers. *Intl J. Numer. Meth. Fluids* **14**, 1087. Also in *AIAA Paper* 90-1531.
- KIM, J. & MOIN, P. 1984 Application of a fractional-step method to incompressible Navier–Stokes equations. *J. Comput. Phys.* **59**, 308.
- KIM, J., MOIN, P. & MOSER, R. 1987 Turbulence statistics in fully developed channel flow at low Reynolds number. *J. Fluid Mech.* **177**, 133.
- KLINE, S. J., REYNOLDS, W. C., SCHRAUB, F. A. & RUNSTADLER, P. W. 1967 The structure of turbulent boundary layers. *J. Fluid Mech.* **30**, 741.
- LAUNDER, B. E. 1990 Phenomenological modelling: present...and future? *Whither Turbulence? Turbulence at the Crossroads* (ed. J. L. Lumley). Lecture Notes in Physics, vol. 357, p. 439. Springer.
- LAUNDER, B. E. & YING, W. M. 1972 Secondary flows in ducts of square cross-section. *J. Fluid Mech.* **54**, 289.
- LE, H. & MOIN, P. 1991 An improvement of fractional step methods for the incompressible Navier–Stokes equations. *J. Comput. Phys.* **92**, 369.
- LUMLEY, J. L. 1991 Order and disorder in turbulent flows. In *New Perspectives in Turbulence*, p. 105. Springer.
- MADABHUSHI, R. K. & VANKA, S. P. 1991 Large eddy simulation of turbulence-driven secondary flow in a square duct. *Phys. Fluids A* **3**, 2734.
- MANSOUR, N. N., KIM, J. & MOIN, P. 1988 Reynolds-stress and dissipation rate budgets in a turbulent channel flow. *J. Fluid Mech.* **194**, 15.
- MOIN, P. & KIM, J. 1982 Numerical investigation of turbulent channel flow. *J. Fluid Mech.* **118**, 341.
- MOIN, P. & MOSER, R. D. 1989 Characteristic-eddy decomposition of turbulence in a channel. *J. Fluid Mech.* **200**, 471.
- MOSER, R. D. & MOIN, P. 1987 The effects of curvature in wall-bounded turbulent flows. *J. Fluid Mech.* **175**, 479.
- NIKURADSE, J. 1930 Turbulente Strömung in nicht kreisförmigen Röhren. *Ing. Arch.* **1**, 306.
- PERKINS, H. J. 1970 The formation of streamwise vorticity in turbulent flow. *J. Fluid Mech.* **44**, 721.
- PRANDTL, L. 1926 Über die ausgebildete Turbulenz. *Verh. 2nd Intl Kong. für Tech. Mech., Zurich*. [English transl. *NACA Tech. Memo.* **435**, 62].
- PRANDTL, L. 1952 *Essentials of Fluid Dynamics*, p. 145. Glasgow: Blackie.
- RAI, M. M. & MOIN, P. 1991 Direct simulation of turbulent flow using finite difference schemes. *J. Comput. Phys.* **96**, 15. Also in *AIAA Paper* 89-0369.
- SPALART, P. R. 1985 Numerical simulation of boundary layers. *NASA TM88220-88222*.
- WILLMARTH, W. W. 1975 Pressure fluctuations beneath turbulent boundary layers. *Ann. Rev. Fluid Mech.* **5**, 13.